Initiating planet formation : the collisional evolution of small dust aggregates

Paszun, D.

Publication date
2008

6

Dust coagulation and fragmentation in molecular clouds

C. W. Ormel, D. Paszun, C. Dominik, A. G. G. M. Tielens
To be submitted

Abstract
The cores in molecular clouds are the densest and coldest regions of the interstellar medium (ISM). These are the places, therefore, where the ISM-dust grains can coagulate. Here, we study the coagulation and fragmentation process from first principles; through direct quantification of the outcomes of detailed numerical simulations that cover a wide parameter space characterized by four dimensions: energy, porosity, angle of impact, and size ratio. Collisions can result in sticking or fragmentation (shattering, breakage, and erosion) and affect the internal structure of the particles. In combination with a Monte Carlo coagulation code the dust aggregate collision model is applied to a homogeneous and static cloud of temperature 10 K and gas densities that range from $n = 10^3$ cm^{-3} to 10^7 cm^{-3}. The coagulation is followed locally for timescales of $\sim 10^7$ yr. We find that the growth can be divided into two stages: a growth-dominated phase and a fragmentation-dominated phase, in which the evolution evolves towards steady state. In the first stage the mass distribution is relatively narrow, peaking at a particular size that shifts to larger size with time. At some point, however, collision velocities are energetic enough to fragment particles, which decrease the growth rate and start to replenish the particles of lower mass. Eventually, a steady state is reached, where the mass distribution is characterized by a relatively flat $m^2 f(m)$ mass-spectrum (equal amount of mass per logarithmic size bin). The amount of growth depends on the density of the gas (setting the coagulation timescale) compared to the lifetime of the cloud, as well as on the material properties of the dust grains. Coagulation between silicates are always in the fragmentation regime, whereas ice-coated particles show a large potential for growth due to their better sticking properties. If clouds evolve on free-fall timescales, however, little coagulation is expected to take place in either case. However, if clouds have long-term support mechanism and live in isolation, the impact of coagulation is important, leading to a significant decrease of the opacity if the fragmentation-dominated phase has not yet been reached.

6.1 Introduction

Dust plays a key role in molecular clouds. Extinction of penetrating FUV photons by small dust grains allows molecules to survive. At the same time, gas will accrete on dust grains forming ice mantles consisting of simple molecules (Tielens and Hagen 1982; Hasegawa et al. 1992; Bergin and Langer 1997). Moreover, surface chemistry provides a driving force towards molecular complex-

ity (Charnley et al. 1992; Aikawa et al. 2008). Dust also plays an active role in the star formation process. The smallest grains set the degree of ionization in the cloud, which controls the ambipolar diffusion rate and therefore regulates the magnetic support of prestellar cores (Ciolek and Mouschovias 1994). Radiation pressure on grains limits the mass accretion onto luminous protostars and hence grains may play a role in the upper mass cut off of stellar masses (Kahn 1974; Wolfire and Cassinelli 1987). Furthermore, after entering a protoplanetary disk, interstellar dust grains also provide building blocks from which ever larger bodies such as chondrules, planetesimals and cometesimals can be built. Finally, dust is often used as a proxy for the total gas (H_2) column density, either through near-IR extinction measurements or through sub-millimeter emission studies (Johnstone and Bally 2006; Alves et al. 2007; Jorgensen et al. 2008). Dust is often preferred as a tracer in these types of studies because it is now well established that – except for pure hydrides – all species condense out in the form of ice mantles at the high densities of prestellar cores (Flower et al. 2006; Bergin and Tafalla 2007; Akyilmaz et al. 2007). Thus, it is clear that our assessment of the molecular contents of clouds, as well as the overall state of the star and planet formation process, are tied to the properties of the dust grains – in particular, its size distribution.

The properties of interstellar dust are, however, expected to change during its sojourn in the molecular cloud phase. In particular, dust grains are expected to grow in size and this has profound influence on many of the processes involving dust. Grain sizes will increase due to the growth of ice mantles but this has only a limited effect because the total ice volume will be dominated by the smallest grains – which dominate the total grain surface area – and, if all the condensible gas freezes out, the thickness of the ice mantles is still only 175 Å, independent of core size (Draine 1985). In dense clouds, coagulation is potentially a much more important promoter of dust growth. Observationally, the decreased visual extinction per H-nucleus in the ρ-Oph cloud is evidence for dust growth by coagulation (Jura 1980). Indirect evidence for grain coagulation is also provided by a comparison of visual absorption studies (e.g., star counts) and sub-millimeter emission studies which imply that the smallest grains have been removed efficiently from the interstellar grain size distribution (Stepnik et al. 2003). On a long time scale ($>10^8$ yr), the interstellar grain size distribution is thought to reflect a balance between coagulation in dense clouds and shattering in interstellar shocks as material constantly cycles between dense and diffuse ISM phases (Jones et al. 1996; O'Donnell and Mathis 1997). Thus, because coagulation controls the total surface area of dust in molecular cloud cores, it in turn affects many of the direct and indirect observational manifestations in these environments.

Because it is the site of planet formation, coagulation studies have largely focused on grain growth in protoplanetary disks (Weidenschilling and Cuzzi 1993). In molecular clouds, dust coagulation has been theoretically modeled by Ossenkopf (1993) and Weidenschilling and Ruzmaikina (1994). In these studies,

coagulation is driven by processes that provide grains with a relative motion. For larger grains ($\gtrsim$100 Å) turbulence in particularly is important in providing relative velocities. These motions – and the outcomes of the collisions – are very sensitive to the coupling of the particles to the turbulent eddies, which is determined by the surface area-to-mass ratio of the dust particles. At low velocities, grain collisions will lead to the growth of very open and fluffy structures, while at intermediate velocities compaction of aggregates will occur. At very high velocities, cratering and even catastrophic destruction will provide a powerful counterforce to the coagulation process (Dominik and Tielens 1997; Paszun and Dominik 2008a; Blum and Wurm 2008). It is clear then that understanding grain growth requires us to know the relationships between the macroscopic velocity field of the molecular cloud, the internal structure of aggregates (which follows from its collision history), and the microphysics of dust aggregates collisions. In view of the complexity of the coagulation process and the then existing, limited understanding of the coagulation process itself, previous studies of coagulation in molecular cloud settings have been forced to make a number of simplifying assumptions concerning the characteristics of growing aggregates.

Theoretically, our understanding of the coagulation process has been much helped by the development of the atomic force microscope, which has provided much insight in the binding of individual monomers. This has been translated into simple relationships between velocities and material parameters, which prescribe under which conditions sticking, compaction, and fragmentation occur (Chokshi et al. 1993; Dominik and Tielens 1997). Over the last decade, a number of elegant experimental studies by Blum and coworkers (e.g., Blum and Wurm 2008) have provided direct support for these concepts and in many ways expanded our understanding of the coagulation process. Numerical simulations have translated these concepts into simple recipes, which link the collisional parameters and the aggregate properties to the structures of the evolving aggregates (Paszun and Dominik 2008a). Together with the development of Monte Carlo methods, in which particles are individually followed (Ormel et al. 2007; Zsom and Dullemond 2008), these studies provide a much better framework for modeling the coagulation process than hitherto possible.

In this paper, we reexamine the coagulation of dust grains in molecular cloud cores in the light of this improved understanding of the basic physics of coagulation with a two-fold goal. First, we will investigate the interrelationship between the detailed prescriptions of the coagulation recipe and the structure, size, and mass of the resulting aggregates. While these collisional recipes are very general, we have elected here to apply them to the relatively simple setting of a molecular cloud core. This will serve as an efficient way to investigate the implication of the detailed collision experiments. In a future study, we may apply these recipes to more convoluted models for the structure of molecular clouds, as well as studying grain growth and planet formation in protoplanetary disks. Second, we will give a simple prescriptions for the temporal evolution of the total grain surface area, thereby capturing its observational characteristics, in

terms of the physical conditions in the core. Because the surface area holds the key to many of the physical effects involving grains in dense cores – including opacity and surface chemistry – we expect that a simple, but reliable, description of the coagulation process will be of great benefit to the larger field of molecular cloud physics.

This paper is organized as follows. In Sect. 6.2 the static cloud model that is adopted for the gas properties is presented and linked to the turbulent velocity structure. Section 6.3 describes the results from the collisional experiments, and quantifies their outcome in the collision recipe. A significant effort is invested to make the outcomes of the numerical collision experiments applicable to a size regime much larger than the collision experiments can handle. Also, the outcome is quantified in such a way to treat a Monte Carlo approach, discussed in Sect. 6.4. In Sect. 6.5 the results are presented: we discuss the imprints of the collision recipe on the coagulation and also present a parameter study, varying the cloud gas densities and the dust material properties. The merits of our approach are discussed in Sect. 6.6, together with some caveats. In Sect. 6.7 we review the implications of our result to molecular clouds. Section 6.8 summarizes the main conclusions of this study.

Table 6.1: List of symbols.

Symbol	Description
$\mathcal{E}^*$	reduced modulus of elasticity
$\mathcal{R}_{\rm gd}$	gas-to-dust ratio by mass
Δv	relative velocity
γ	surface energy density
$\delta_{\rm c}$	critical displacement length
$\delta_{\rm e}$	equilibrium displacement length
η	number of particles or groups (Sect. 6.4.1)
μ	molecular mass
$\nu_{\rm m}, \nu_{\rm t}$	molecular, turbulent viscosity
$\xi_{\rm crit}$	critical displacement for irreversible rolling
ρ_0	material density, $\rho_0 = 2.65$ g cm^{-3} (silicates), $\rho_0 = 1.0$ g cm^{-3} (ice)
$\rho_{\rm g}$	gas density, $\rho_{\rm g} = \mu n m_{\rm H}$
σ	average projected surface area
$\sigma_{12}^{\rm C}$	collisional cross section
$\tau_{\rm f}$	friction time
C_ϕ	change in geometrical filling factor, $C_\phi = \phi_\sigma / \phi_\sigma^{\rm ini}$
$D_{\rm f}$	fractal dimension
E	collision energy, $E = \frac{1}{2} m_\mu (\Delta v)^2$
$E_{\rm roll}$	rolling energy, $E_{\rm roll} = 3\pi^2 \gamma \xi_{\rm crit} (a_0/2)$
$E_{\rm br}$	breaking energy
$F_{\rm c}$	pull-off force
N	number of grains in aggregate (dimensionless measure of mass)
N_μ	reduced number of monomers in collision $N_\mu = N_1 N_2 / (N_1 + N_2)$
$N_{\rm f}$	number of big fragments
$N_{\rm tot}$	total number of monomers in aggregates
$M_{\rm f}$	mass in big fragment component
$M_{\rm pwl}$	mass in power-law component
Re	Reynolds number
$S_{\rm f}$	spread in number of fragments of big component
St	particle Stokes number
T	temperature
a_0	monomer radius
$a_{\rm out}$	aggregate outer radius
a_σ	aggregate geometrical radius (projected surface equivalent radius)
a_μ	reduced radius
$a_{\rm e}$	equilibrium contact radius
b	impact parameter
$c_{\rm g}$	sound speed (gas)
$f_{\rm miss}$	fraction of collision misses
$f_{\rm pwl}$	fraction of mass in power-law component
n	particle density (gas)
m	particle mass
m_μ	reduced mass of collision
$m_{\rm H}$	hydrogen mass
q	power-law exponent (size distribution)
$t_{\rm s}$	inner (Kolmogorov) eddy turn-over time
$v_{\rm L}$	large eddy turn-over velocity
$v_{\rm br}$	critical breaking velocity.
$v_{\rm s}$	inner (Kolmogorov) eddy turn-over velocity

6.2 Density and velocity structure of molecular clouds

The physical structure – the gas density and temperature profiles – of molecular clouds is determined by its support mechanisms. Various support mechanisms can be envisioned: thermal, rotation, magnetic fields, or turbulence. If there is only thermal support to balance the cloud's self-gravity and the temperature is constant, its structure is that of an isothermal sphere where the gas density ($\rho_{\rm g}$) falls-off with radius (r) as $\rho_{\rm g} \propto r^{-2}$. However, the isothermal sphere is unstable as it heralds the collapse phase (Shu 1977). The cloud will then collapse on a free-fall timescale

$$t_{\rm ff} = \sqrt{\frac{3\pi}{32 G \rho_{\rm g}}} = 1.1 \times 10^5 \ {\rm yr} \left(\frac{n}{10^5 \ {\rm cm}^{-3}} \right)^{-1/2}, \tag{6.1}$$

where G is Newton's gravitational constant, $n = \rho_{\rm g}/m_{\rm H}\mu$ the number density of the molecular gas with $m_{\rm H}$ the hydrogen mass and μ the molecular mass $\mu = 2.34$. Thermally supported cores are only stable if the thermal pressure wins over gravity, a situation described by the Bonnor-Ebert sphere (still assuming a constant temperature), where an external pressure confines the cloud. The critical Bonnor-Ebert mass is (Ebert 1955; Bonnor 1956)

$$M_{\rm BE} = c_{\rm BE} \frac{c_{\rm g}^4}{P_{\rm out}^{1/2} G^{3/2}}, \tag{6.2}$$

where $c_{\rm g}$ is the isothermal sound speed, $P_{\rm out}$ the external pressure, and $c_{\rm BE} \simeq 1.18$. Inserting $P_{\rm out} = \rho_{\rm g} c_{\rm g}^2$, $c_{\rm g}^2 = kT/\mu$ and $\rho_{\rm g} = n\mu m_{\rm H}$ we obtain

$$M_{\rm BE} = c_{\rm BE} \frac{c_{\rm g}^3}{G^{3/2} \sqrt{n \mu m_{\rm H}}} = 0.31 \ M_\odot \left(\frac{T}{10 \ {\rm K}} \right)^{3/2} \left(\frac{n}{10^5 \ {\rm cm}^{-3}} \right)^{-1/2}, \tag{6.3}$$

where, n is the density at the outer radius of the cloud. Because Bonnor-Ebert spheres have a modest density gradient, the density in the center of the core is a factor of ~10 larger. Thermally-supported subcritical Bonnor-Ebert spheres ($M \lesssim M_{\rm BE}$) are stable and can in principle exist on long timescale – as long as they are not disturbed by dynamical interactions.

Magnetic fields in particular are important to support the cloud against the opposing influence of gravity, because the ions, which are tied to the field, will prevent the cloud from collapsing. Ion-molecule collisions will move the magnetic field out of the cloud, which can be a prolonged process. The ambipolar diffusion timescale can be estimated from the ion-molecular collision rate, $K_{in} \sim 2 \times 10^{-9}$ cm^3 s^{-1}. The force on a neutral particle through momentum transfer due to collisions with ions is $F_{\rm ad} = m_{\rm n} v_{\rm dr} K_{in} n_i$, where $m_{\rm n}$ is the neutral mass, $v_{\rm dr}$ the ion-molecule drift velocity, and n_i the number density in ions. This force

balances the gravitational force, from which the drift velocity can be obtained. The ambipolar diffusion timescale, $t_{\rm ad} = r/v_{\rm dr}$, then becomes,

$$t_{\rm ad} = \frac{3K_{in}}{4\pi\mu m_{\rm H} G}\left(\frac{n_i}{n}\right) \simeq 3.7\times10^6 \text{ yr}\left(\frac{n}{10^5 \text{ cm}^{-3}}\right)^{-1/2}, \tag{6.4}$$

where we have assumed a degree of ionization due to cosmic rays of $n_i/n = 2\times10^{-5}/\sqrt{n}$ (Tielens 2005).

Turbulence is another possible support mechanism of molecular cores, but its nature is dynamic – rather than (quasi)static. At large scales it provides global support to molecular clouds, whereas at small scales it locally compresses the gas. If these overdensities exist on timescales of Eq. (6.1), collapse will follow. This is the gravo-turbulent fragmentation picture of turbulence-dominated molecular clouds, where the (supersonic) turbulence is driven at large scales, but also reaches the scales of quiescent ($\sigma_{\rm turb} < c_{\rm g}$) cores (Mac Low and Klessen 2004; Klessen et al. 2005). In this dynamical, turbulent-driven picture both molecular clouds and cores are transient objects.

Thus, cloud cores will dynamically evolve due to either ambipolar diffusion and loss of supporting magnetic fields or due to turbulent dissipation, or simply because the core is only a transient phase in a turbulent velocity field. In this work, for reasons of simplicity, we constrain ourselves to a static cloud model, where turbulence is unimportant for the support of the core, but we do include (subsonic) turbulence in the formalism for the calculation of relative motions between the dust particles. In the following we present the working model for the structure of the cloud.

6.2.1 Working model

In this exploratory study we will for simplicity adopt an homogeneous core of mass given by the critical Jeans mass. Moreover, we assume the cloud is turbulent, but neglect the effects the turbulence has for the support of the cloud. Thus, our approximation is probably applicable for high density, low mass cores as velocity dispersions increase towards high mass cores (Kawamura et al. 1998). The homogeneous structure causes collision timescales to be the same throughout the cloud, i.e., the coagulation and fragmentation is treated locally and not affected by diffusion. In our calculations, we will study the sensitivity of the coagulation process on the gas density n and compare the calculated coagulation/fragmentation timescales to the other relevant timescales in the problem.

Starting from the isodense sphere, we derive the turbulent velocity structure. First, the cloud outer radius is given by the Jeans length (Binney and Tremaine 1987)

$$L_{\rm J} = \frac{1}{2}\sqrt{\frac{\pi v_{\rm g}^2}{G\rho_{\rm g}}} = 0.033 \text{ pc}\left(\frac{n}{10^5 \text{ cm}^{-3}}\right)^{-1/2}\left(\frac{T}{10 \text{ K}}\right)^{1/2}, \tag{6.5}$$

From which the Jeans mass is obtained as

$$M_{\rm J} = \frac{4\pi}{3}\rho_{\rm g} L_{\rm J}^3 = 0.90\ M_\odot \left(\frac{n}{10^5\ {\rm cm}^{-3}}\right)^{-1/2} \left(\frac{T}{10\ {\rm K}}\right)^{3/2}. \tag{6.6}$$

and the sound crossing time of the core is

$$t_{\rm cross} = \frac{L_{\rm J}}{c_{\rm g}} = 1.7 \times 10^5\ {\rm yr} \left(\frac{n}{10^5\ {\rm cm}^{-3}}\right)^{-1/2}, \tag{6.7}$$

independent of temperature. At the Jeans mass, the crossing time is of course equal to the free-fall time of the cloud.

We now assume *(i)* that the largest eddies decay on the sound crossing time of Eq. (6.7) (i.e., $t_{\rm L} = t_{\rm cross}$), and *(ii)* that the fluctuating velocity at the largest scale is given by the sound speed i.e., $v_{\rm L} = c_{\rm g}$. Thus, the turbulent viscosity is $\nu_{\rm t} = L v_{\rm L} = v_{\rm L}^2 t_L = c_{\rm g} L_{\rm J}$ with $L = L_{\rm J}$ the size of the largest eddies. Although our parameterization of the large eddy quantities seems rather ad-hoc, we can build some trust in this relation by considering the energy dissipation rate $v_{\rm L}^3/L$ per unit mass. Balancing the energy dissipation with the heating, requires a heating rate $n\Gamma$ of

$$n\Gamma = \frac{v_L^3}{L}\rho_{\rm g} = 2.5 \times 10^{-23}\ {\rm erg\ cm^{-3}\ s^{-1}} \left(\frac{T}{10\ {\rm K}}\right)\left(\frac{n}{10^5\ {\rm cm}^{-3}}\right)^{3/2}. \tag{6.8}$$

Based upon observational studies of turbulence in cores, Tielens (2005) give a heating rate of $n\Gamma = 3 \times 10^{-28} n$ erg s^{-1}, with which Equation (6.8) reasonably agrees for the range of densities we will consider. Additionally, the adoption of the crossing time and sound speed for the large eddy properties are natural upper limits. A higher value for the sound speed means that turbulence becomes supersonic, which may be difficult to sustain. A much reduced value, on the other hand, would give an energy dissipation that may be too low. Note again that turbulence does not act as a support mechanism in our working model.

The turbulent properties further follow from the Reynolds number, which is the ratio of the turbulent viscosity ν_t over the molecular viscosity ν_m,

$$Re = \frac{\nu_{\rm t}}{\nu_{\rm m}} = \frac{v_{\rm L} L}{c_{\rm g}\ell_{\rm mfp}/3} = 6.2 \times 10^7 \left(\frac{n}{10^5\ {\rm cm}^{-3}}\right)^{1/2} \left(\frac{T}{10\ {\rm K}}\right)^{1/2}, \tag{6.9}$$

where $\nu_{\rm m}$ is the molecular viscosity and $\ell_{\rm mfp}$ the mean free path of a gas particle. Assuming a Kolmogorov cascade, the turn-over time and velocity at the inner scale follow from the Reynolds number as,

$$t_{\rm s} = Re^{-1/2} t_{\rm L} = 2.2 \times 10^2\ {\rm yr} \left(\frac{n}{10^5\ {\rm cm\ s^{-1}}}\right)^{-3/4} \left(\frac{T}{10\ {\rm K}}\right)^{-1/4} \tag{6.10}$$

$$v_{\rm s} = Re^{-1/4} v_{\rm L} = 2.1 \times 10^2\ {\rm cm\ s^{-1}} \left(\frac{n}{10^5\ {\rm cm\ s^{-1}}}\right)^{-1/8} \left(\frac{T}{10\ {\rm K}}\right)^{3/8}. \tag{6.11}$$

We note that the fluctuating velocity of the smallest eddies is a few m/s.

6.2.2 Relative velocities between dust particles

The quantity that determines the amount of interaction a particle experiences with the gas is the friction time $\tau_{\rm f}$,

$$\tau_{\rm f} = \frac{3}{4\pi c_{\rm g}\rho_{\rm g}}\frac{m}{\sigma}, \tag{6.12}$$

where m is the mass of the particle and σ the average projected surface area. For compact grains of size a_0 and density ρ_0, Eq. (6.12) scales linearly with radius, $\tau_{\rm f} = a_0\rho_0/c_{\rm g}\rho_{\rm g}$. However, for porous particles σ can have a much steeper dependence on mass (in the case of flat structures, $\sigma \propto m$) and $\tau_{\rm f}$ a much weaker dependence.

Ossenkopf (1993) considers a variety of sources for inducing relative velocities between dust particles in molecular clouds: asymmetric drift velocities, Brownian motion, gravitational settling, and turbulence. Except for combinations of high densities and small particles, turbulence dominates the velocity field between the particles. This becomes clear from considering the friction time of particles of radius a_0

$$\tau_0 = \tau_{\rm f}(a_0) = \frac{\rho_0 a_0}{c_{\rm g}\rho_{\rm g}} = 1.1\times10^2\ {\rm yr}\left(\frac{n}{10^5\ {\rm cm^{-3}}}\right)^{-1}\left(\frac{T}{10\ {\rm K}}\right)^{-1/2}\left(\frac{a_0}{0.1\ \mu{\rm m}}\right), \tag{6.13}$$

where we take the bulk density $\rho_0 = 2.65$ g cm^{-3} applicable to silicates. Specifically, the '0' subscript denotes the smallest constituent dust particle (monomer). Because $\tau_0 > t_{\rm s}$ the particle motion will not align with the eddies of shorter turnover time. These 'class II' eddies (Voelk et al. 1980) are responsible for giving random kicks to the particle motion | an important source for sustaining relative velocities of at least $\Delta v \sim v_{\rm s}$. These velocities are rather insensitive to density as *(i)* $v_{\rm s}$ has a very shallow dependence on n; and *(ii)* the ratio $\tau_{\rm f}/t_{\rm s}$, which we define as the Stokes number ${\rm St_s}$[1] is also weakly dependent on density

$${\rm St_s} \equiv \frac{\tau_{\rm f}}{t_{\rm s}} = 5.2\left(\frac{a_0}{0.1\ \mu{\rm m}}\right)\left(\frac{n}{10^5\ {\rm cm^{-3}}}\right)^{-1/4}\left(\frac{T}{10\ {\rm K}}\right)^{-1/4}. \tag{6.14}$$

It is only for densities above $\sim10^7$ cm^{-3} that 10^{-5} cm size dust grains have ${\rm St_s} < 1$. Specifically, for identical particles of ${\rm St_s} > 1$, $\Delta v \approx \sqrt{3}v_{\rm s}{\rm St_s}^{1/2}$ (Ormel and Cuzzi 2007). The relative velocity between two dust monomers is then

$$\Delta v_0 \approx \sqrt{3}v_{\rm s}{\rm St_s}^{1/2} = 8.3\times10^2\ {\rm cm\ s^{-1}}\left(\frac{a_0}{0.1\ \mu{\rm m}}\right)^{1/2}\left(\frac{n}{10^5\ {\rm cm^{-3}}}\right)^{-1/4}\left(\frac{T}{10\ {\rm K}}\right)^{1/4}. \tag{6.15}$$

Thus, velocities between silicate dust particles are $\sim$10 m/s, and decrease only very slowly with density. The same expression holds when the silicates are coated by an ice mantle that is not too thick, as we will assume throughout this

[1] The more usual definition is ${\rm St} = \tau_{\rm f}/t_{\rm L}$.

Table 6.2 — Collision outcome predicted by Dominik and Tielens (1997) for 2d aggregates. The breaking energy, $E_{\rm br}$, corresponds to the energy to break a single contact, whereas the rolling energy, $E_{\rm roll}$, corresponds to the energy required for visible restructuring of the contact area through rolling. The number of contacts in an aggregate, denoted by $N_{\rm c}$, is typically similar to the number of monomers the aggregate contains, N.

Energy	Outcome of Collision
$E < 5E_{\rm roll}$	Sticking without restructuring
$E \approx 5E_{\rm roll}$	Onset of restructuring local to the impact area
$E \approx N_{\rm c}E_{\rm roll}$	Maximum compression
$E \approx 3N_{\rm c}E_{\rm br}$	Onset of erosion (start to lose monomers)
$E > 10N_{\rm c}E_{\rm br}$	Catastrophic disruption

paper (i.e., ρ_0 is then still the silicate bulk density). Dust monomers then collide on a collision timescale of

$$t_{\rm coll,0} = \left(n_{\rm d}\Delta v_0 4\pi a_0^2\right)^{-1} = \frac{\rho_0 a_0 \mathcal{R}_{\rm gd}}{3\rho_{\rm g}\Delta v_0} = 8.5{\times}10^4\ {\rm yr}\left(\frac{a_0}{0.1\ \mu{\rm m}}\right)^{1/2}\left(\frac{n}{10^5\ {\rm cm}^{-3}}\right)^{-3/4}\left(\frac{T}{10\ {\rm K}}\right)^{-1/4}, \tag{6.16}$$

where $\mathcal{R}_{\rm gd} = 100$ is the standard gas-to-dust density ratio by mass. Thus, if dense cores exist on timescales less then Eq. (6.16) coagulation is of little importance. This happens, e.g., when the cores exist on free-fall timescales (Eq. (6.1)) at densities less than $n = 10^4$ cm^{-3}. On the other hand, if the lifetime of molecular clouds is longer than Eq. (6.16) we do expect that coagulation is significant. At very high densities ($n \gg 10^5$ cm^{-3}) $t_{\rm coll,0}$ can become much less than the lifetime of the core – especially if long term support mechanisms are available – and we do therefore expect significant potential for coagulation.

6.2.3 Particle sticking, restructuring and fragmentation

Although a detailed model for the outcome of collisional encounters between dust aggregates will be discussed in Sect. 6.3, it is instructive to present order-of-magnitude expressions for the sticking behavior of dust aggregates. This requires us to compare the critical threshold for sticking with the expected relative velocity between two dust particles derived above.

Dominik and Tielens (1997) provide a simple recipe for the outcome of aggregate collisions, see Table 6.2. According to Dominik and Tielens (1997) the outcome of a collision depends on the impact energy,

$$E = \frac{1}{2}m_\mu(\Delta v)^2, \tag{6.17}$$

where m_μ is the reduced mass, relative to two critical energy thresholds: the energy required to break a contact, $E_{\rm br}$, and the energy required to roll a contact,

$E_{\rm roll}$. From the Dominik and Tielens (1997) study,

$$E_{\rm br} = A_{\rm br}\frac{\gamma^{5/3}a_\mu^{4/3}}{\mathcal{E}^{\star\,2/3}}; \tag{6.18a}$$

$$E_{\rm roll} = 6\pi^2\xi_{\rm crit}\gamma a_\mu, \tag{6.18b}$$

where $a_\mu = a_1a_2/(a_1 + a_2)$ is the reduced radius of the aggregates colliding (in our case we shall always consider two equal-size monomers such that $a_\mu = a_0/2$), and γ and $\mathcal{E}^\star$ are, respectively, the surface energy density and the reduced elastic modulus of the material. The model parameters $\xi_{\rm crit}$ and $A_{\rm br}$ result from the Dominik and Tielens (1997) study: $\xi_{\rm crit} = 10^{-8}$ cm and $A_{\rm br} = 43$. The critical energies of Eq. (6.18) were obtained by Dominik and Tielens (1997) from theoretical considerations; however, laboratory experiments performed by Poppe et al. (2000) showed that monomers stick at a much higher velocity than predicted from the derived theoretical limit. Although the nature of this discrepancy remains unclear, the constant $A_{\rm br}$ in Eq. (6.18a) had to be increased by about two orders of magnitude. Moreover, Heim et al. (1999) find that the energy $E_{\rm roll}$ is also an order of magnitude higher than the threshold given by the theory. This indicates that the critical displacement $\xi_{\rm crit}$ must be about 10 times larger than assumed by Dominik and Tielens (1997). Blum and Wurm (2000), however, confirmed the quantitative picture proposed by the theory, provided that the experimental threshold energies are used ($\xi_{\rm crit} = 2\times10^{-7}$ cm and $A_{\rm br} = 2.8\times10^3$). In this study we will adopt these experimentally-measured values.

Using the critical energies, we briefly review contact breaking and restructuring. Contact breaking occurs when $E > E_{\rm br}$, where E is the collision energy. The critical velocity is therefore,

$$\begin{aligned} v_{\rm br} &= \sqrt{\frac{2E_{\rm br}}{m_\mu}} = \sqrt{2A_{\rm br}}\frac{\gamma^{5/6}a_\mu^{4/6}}{\mathcal{E}^{\star\,1/3}m_\mu^{1/2}} = \sqrt{\frac{6A_{\rm br}}{4\pi}}\rho_0^{-1/2}\gamma^{5/6}a_\mu^{2/3}a_0^{-3/2}\mathcal{E}^{\star\,-1/3} \\ &= 7.4\ {\rm m\ s^{-1}}\ N_\mu^{-1/2}\left(\frac{a_\mu}{a_0}\right)^{2/3}\left(\frac{a_0}{0.1\ \mu{\rm m}}\right)^{-5/6}\left(\frac{\rho_0}{2.65\ {\rm g\ cm^{-3}}}\right)^{-1/2} \\ &\quad\times\left(\frac{\gamma}{25\ {\rm erg\ cm^{-2}}}\right)^{5/6}\left(\frac{\mathcal{E}^\star}{2.8\times10^{11}\ {\rm dyn\ cm^{-2}}}\right)^{-1/3}. \end{aligned} \tag{6.19}$$

In this expression we have introduced the reduced number of monomers in the collision, $N_\mu = N_1N_2/(N_1 + N_2) = m_\mu/m_0$ and inserted the material properties measured for small silicate grains. Given the expected velocities in molecular cores we see that breaking of contacts is important for silicate grains of 0.1 μm. However, ice formation on the surface of dust particles will change this picture. Adhesion forces are governed in this case by the material properties of ice, where the surface energy density is $\gamma = 370$ erg cm^{-2} and the reduced elasticity modulus is $\mathcal{E}^\star = 3.7\times10^{10}$ dyn cm^{-2}. This results in a higher velocity threshold of $v_{\rm br} = 1.2\times10^4$ cm s^{-1} between two monomers. However, in aggregates the

collisional energy is distributed over multiple monomers so that a more realistic threshold for shattering is $E \sim N_c E_{\rm br}$, even increasing the threshold for fragmentation. Besides, the collisional energy can also be dissipated by restructuring. From these considerations it is clear that for ices (or ice-coated silicates) high velocities, $>10^2$ m s^{-1}, are required to fully fragment aggregates. There are two exceptions, however. In very fluffy fractal aggregates that have an open structure (e.g., string-like), removal of a central contact may result in its breakup. Secondly, if the impact energy is localized in a small region of the aggregate we may expect that collisions of velocity $v \gtrsim v_{\rm br}$ produce some local damage in the form of cratering. This local aspect will feature prominently in the collision recipe of Sect. 6.3.

At collision energies less than the restructuring limit, $E < 5E_{\rm roll}$, aggregates collide without affecting their internal structure. Then, the collision is in the 'hit-and-stick' regime (Blum and Wurm 2000). Translating the collision energy to a velocity thresholds gives

$$v_{\rm hs} = \sqrt{\frac{10E_{\rm roll}}{m_\mu}} = \sqrt{45\pi}\, a_\mu^{1/2} a_0^{-3/2} \rho_0^{-1/2} \xi_{\rm crit}^{1/2} \gamma^{1/2} N_\mu^{-1/2}$$
$$= 16.3 \text{ m s}^{-1}\, N_\mu^{-1/2} \left(\frac{a_\mu}{a_0}\right)^{1/2} \left(\frac{a_0}{0.1\ \mu\text{m}}\right)^{-1} \left(\frac{\rho_0}{2.65 \text{ g cm}^{-3}}\right)^{-1/2} \left(\frac{\gamma}{25 \text{ erg g}^{-1}}\right)^{1/2}. \quad (6.20)$$

It should be noted that Eq. (6.20) is applicable to aggregates, whereas Eq. (6.19) gives the breaking velocity between two monomers. Because we consider aggregates, we give preference to the $v_{\rm hs}$ threshold (even though it is in the case of silicates higher than $v_{\rm br}$), which has been experimentally verified as the onset for restructuring (Blum and Wurm 2000).

Comparing the critical sticking velocities (Eqs. (6.19), (6.20)) with the velocities in the molecular cloud (Eq. (6.15)), we may expect that collisions between silicate aggregates are prone to fragmenting behavior from the outset, whereas for ices the onset of fragmentation is delayed – if enough time is available – to a stage where particles are much larger, compact, and have much larger relative velocities. Concerning the structure of aggregates, we expect that restructuring will be important from the outset as $\Delta v \gtrsim v_{\rm hs}$, except perhaps at the highest densities. For ices Eq. (6.20) is a factor of 4 higher, but note that the discrepancy between ice and silicates is less for the rolling energy than for the breaking energy (Eq. (6.18)). Finally, if fragmentation is present, a significant injection of porous material can be expected (see below).

These considerations present, however, only a qualitative picture, which neglects important parameters that may be key to the outcome of the collision, i.e., the particle porosity and the impact parameter. It may therefore be dangerous to provide a full collision model from these energy considerations alone. For a quantitative model, therefore, we will use the results of detailed numerical simulations for collisions between two colliding aggregates, which have been recently performed (Paszun and Dominik 2008a). We will review these numeri-

cal experiments in the next chapter and provide a collision recipe that quantifies their outcome and can be applied to a Monte Carlo coagulation model.

6.3 Collision model

Collisions between aggregates are modeled using the soft aggregates numerical dynamics (SAND) code (Dominik and Nübold 2002; Paszun and Dominik 2008b). This code treats interactions between individual monomers held together by the surface forces in a contact area (Johnson et al. 1971; Derjaguin et al. 1975). The SAND code calculates the equation of motion for each grain individually and simulates vibration, rolling, twisting and sliding of the monomers that are in contact. These interactions lead to energy dissipation via different channels. When two monomers in contact are pulled away, the connection may break causing loss of the energy. Monomers may also roll or slide over each other, which also involves energy dissipation. These mechanisms are discussed in details by Dominik and Tielens (1995, 1996) and Dominik and Tielens (1997). For further details regarding this model and testing it against laboratory experiments we refer the reader to the paper by Paszun and Dominik (2008b).

6.3.1 Collision setup

To understand mechanisms that determine a collision outcome, we performed a large number of simulations covering a wide parameter space. Although all simulations are described in detail by Paszun and Dominik (2008a) we present here a setup of these numerical experiments and provide a qualitative picture of the mechanisms that influence the outcome of a collision.

The outcome of a collision is shaped by five key parameters: *(i)* the collision energy E, *(ii)* the impact parameter b, *(iii)* the initial compactness of aggregates, *(iv)* the mass ratio N_1/N_2, and *(v)* the material properties of the monomers. Using an appropriate normalization, we can describe the collisional outcome independently of the latter parameter (the material properties) so that only four parameters are left. The applied scaling is discussed in Sect. 6.3.5. An example of the setup of a simulation is shown in Fig. 6.1. It illustrates three parameters that determine the outcome of a collision: the initial compactness as represented by the *geometrical* filling factor ϕ_σ (see below), the collision energy E, and the impact parameter b.

A collision for each parameter set is repeated 6 times at different orientations. This provides an overview of the possible range of outcomes. However, some orientations do not result in a collision hit. This is caused by the high porosity of aggregates, where a small particle can fly through voids in a larger aggregate without colliding with it, or, more simply, if the path of the protuberances that characterize fractal, fluffy aggregates do not cross. The fraction of these missing collisions depends on two parameters: the structure of the particle characterized by the geometrical filling factor and the impact parameter.

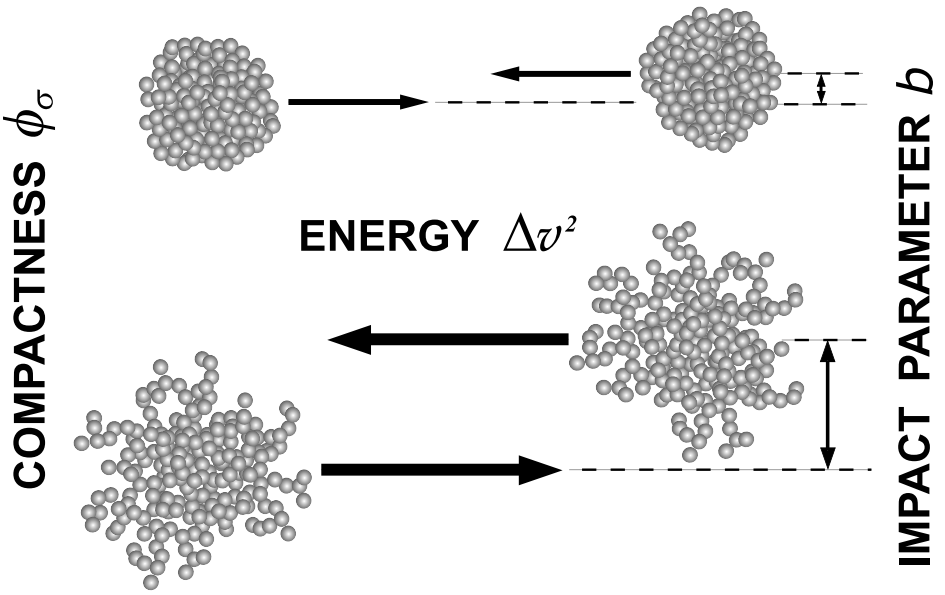

Figure 6.1 — Sketch of the initial setup of our simulations. Different parameters are shown in the plot. We varied collision energy, impact parameter, and compactness.

The range of the parameters we use in our study is summarized in Table 6.3. We sample the collisional energy parameter space from the pure hit-and-stick collisions, where particles grow without changing the internal structure of the colliding aggregates, up to catastrophic destruction, where the aggregate is shattered into small fragments. In the intermediate energy regime, we observe restructuring, where the growth process leads also to a change of the internal structure of an aggregate.

The dimensionless impact parameter space is also well sampled. We probe central collision ($b = 0$), where aggregates can be compressed, grazing impacts ($b \sim 1$), where particles can be stretched due to inertia, and several intermediate cases. The impact parameter is taken relative to the outer radius of the particles, $b_{\max} = a_{\text{out},1} + a_{\text{out},2}$. Here the outer radius a_{out} is the radius of the smallest sphere centered at the center-of-mass of the particle that fully encloses it.

The third parameter that determines the collision outcome is the mass ratio. To verify its influence on a collision outcome, we simulate impacts of different mass aggregates onto a target made of 1000 monomers. In this way we explore the mass ratio in the range from 1 to 10^{-3}. Additional experiments are performed at a mass ratio of unity containing aggregates made of 200 monomers each. The two extreme cases (mass ratio of 1 and 10^{-3}) will affect the outcome of the collision in two qualitatively distinct ways. In collisions between equal-size aggregates the properties of the particle change *globally*, whereas if the colliding particles have very different masses the impact of the collision can be described

Table 6.3 — Parameters used in the numerical simulations. Note that not all combinations are sampled.

v [m/s]	$b/b_{\max}$	mass ratio	ϕ_σ
0.05	0.0	1.0	0.070
0.30	0.25	0.8	0.090
0.50	0.5	0.6	0.122
0.75	0.75	0.4	0.127
1.0	0.875	0.2	0.155
2.0	0.95	0.1	0.161
4.0		0.05	0.189
6.0		0.01	0.251
8.0		0.001	
10.0			

locally (except if the collision energy is very high, see below) The intermediate cases may be classified into one of the two categories of collisions (see below).

The last, fourth, parameter is the initial compactness. To express the compactness of an aggregate we use the geometrical filling factor, defined as

$$\phi_\sigma = N\left(\frac{a_0}{a_\sigma}\right)^3, \tag{6.21}$$

where $a_\sigma = \sqrt{A/\pi}$ is the projected surface equivalent radius. The projected surface area, πa^2, is averaged over a large number of different orientations of the particle. The compactness parameter ϕ_σ is the inverse of the enlargement factor ψ adopted as the structural parameter in the study by Ormel et al. (2007). Although the friction time τ_f follows easily from the geometrical filling factor, it is not straightforward to determine the outer radius a_out of an aggregate based on this quantity. The outer radius is of importance because it determines the collisional cross section (uncorrected for missing collisions) between the aggregates. Therefore, a relation between the radii (a_out and a_σ) has to be provided, see Sect. 6.3.4.

The parameter space of the filling factor ϕ_σ is chosen such that we sample both very porous, fractal aggregates that grow due to the Brownian motion (Krause and Blum 2004; Paszun and Dominik 2006), through intermediate compactness aggregates that form by particle-cluster aggregation (PCA), up to compact aggregates that may result from collisional compaction events. It is not trivial to assign an upper limit for collisional compaction of an aggregate, as unilateral compression is countered by sideways spreading of monomers. Although the upper limit for collisional compression is that of random packing (66%) here, following Ormel et al. (2008a), we use $\phi_\sigma = 33\%$ for the upper limit of (rolling) compression, which is in turn based on laboratory findings of Blum and Schräpler (2004). The compactness influences the collisional output in a few different ways. These are described in Sect. 6.3.2, where we discuss the prescrip-

tion for a collision outcome.

6.3.2 Collision recipe: an overview

To provide both a qualitative and a quantitative description of a collision, Paszun and Dominik (2008a) perform a large number of simulations exploring an extensive parameter space. They formulate a simple, quantitative, collision recipe that determines the influence of the kinetic energy, compactness, and mass ratio on the outcome of aggregate-aggregate collisions. The outcomes of a collision are averaged over the impact parameter b. In this case the contribution from off-center impacts is dominant. The fragment size distribution consists in such a case of two main components: large fragments are produced at large impact parameter collisions and small fragments form mostly in central impacts. An offset hit leads to a very limited interaction that may result in an outcome very similar to the initial setup (two large fragments of weakly changed structure). Moreover, collisions at large b have a higer probability to miss than porous aggregates. Central impacts, on the other hand, are less likely to miss and lead to a better distribution of energy in aggregates. Therefore, collisions at energies above the fragmentation threshold produce many small particles.

For an impact energy above the restructuring energy threshold, a different impact parameter results in a different outcome. In head-on impacts monomers are pushed into the center of an aggregate, filling the pores and compressing the aggregate. On the other hand, in offset collisions, the overlap of interacting aggregates is smaller, and the amount of compression is limited. In this case monomers are pushed further from the center of an aggregate and an elongated particle may be produced. Therefore, tensile forces present in off-center impacts lead to stretching, *decompressing* the agglomerates.

In this paper we reformulate the recipe to probe directly the effect of the impact parameter on the collision evolution of dust aggregates. In this way we explicitly resolve the effects of off-center impacts and compare this to the simplified case of head-on collisions only. Therefore, the recipe becomes four-dimensional and depends on the impact energy, initial compactness, the impact parameter, as well as mass-ratio. The complete presentation of the redesigned recipe is discussed in Sect. 6.3.3.

Given the level of complexity, it is not feasible to provide simple analytical expressions for the outcome parameters of Table 6.4 as function of the collision parameters $(E, \phi_\sigma, b, N_1/N_2)$. Therefore, like in Paszun and Dominik (2008a), the results are expressed in a tabular form, where each table provides one of the output quantities as a function of a normalized collision energy ε and initial filling factor $\phi_\sigma^{\rm ini}$. The exception is the fraction of missed collisions, $f_{\rm miss}$, which is given as function of $a_{\rm out}/a_\sigma$, instead of ϕ_σ. Since the recipe contains a large number of tables we provide them in a digital form only.[2] See Appendix 6.8 for

[2]These tables will be presented as *online material* once this manuscript is submitted to the journal. In Appendix 6.8 we provide an example of the structure of these tables.

further discussion on the format of the collision recipe.

In this study the reshaped recipe is applied to the Monte Carlo model developed by Ormel et al. (2007). This method resolves individual collisions and includes structural parameters. Therefore, our recipe may be easily implemented to study both coagulation and compression of aggregates. In addition, our recipe broadens the range of models, where it can be applied to. The original formulation by Paszun and Dominik (2008a) was designed for applications to continuous methods. Here, the method is extended to become applicable to the particle-oriented approach of the MC method.

6.3.3 Porting the recipe to a Monte Carlo model

An outcome of a collision consists of two essential parts: the mass distribution and the compactness of aggregates in this mass spectrum. The new implementation of our recipe provides these two elements of a collision product in a different form than the original recipe formulated by Paszun and Dominik (2008a). In this study we use the impact parameter as one of the input quantities. Therefore, as discussed above, collision outcomes are not averaged over impact parameter. Additionally, the nature of the Monte Carlo approach requires us to treat discrete quantities. Two components characterize the mass distribution of a collision experiments: *(i)* a power-law component that describes the small fragments and, *(ii)* a large fragment component (one or two fragments). The border line between the two components is at a quarter of the total mass $N_{\rm tot}$. The power-law distribution spans the range from monomer mass up to the $N = 0.25N_{\rm tot}$, while the second component consists of aggregates larger than $0.25N_{\rm tot}$. In this work, the large fragment component is described by different parameters than in Paszun and Dominik (2008a), where a Gaussian distribution was used. In the new recipe we provide a number of large fragments $N_{\rm f}$ with a standard deviation $S_{\rm f}$. The spread in the number of large fragments is found by averaging several simulations performed at different orientations for the same set of parameters.

Table 6.4 presents all quantities describing a collision outcome. The first one

Table 6.4 — Quantities provided by the Monte Carlo suited recipe.

Symbol	Description
$f_{\rm miss}$	Fraction of collisions that resulted in a miss
$N_{\rm f}$	Mean number of large fragments
$S_{\rm f}$	Standard deviation of the $N_{\rm f}$
$f_{\rm pwl}$	The fraction of the total mass (N_1 + N_2) in the small fragments component
q	Exponent of the power-law distribution of small fragments
$C_\phi = \phi_\sigma/\phi_\sigma^{\rm ini}$	Relative change of the geometrical filling factor.

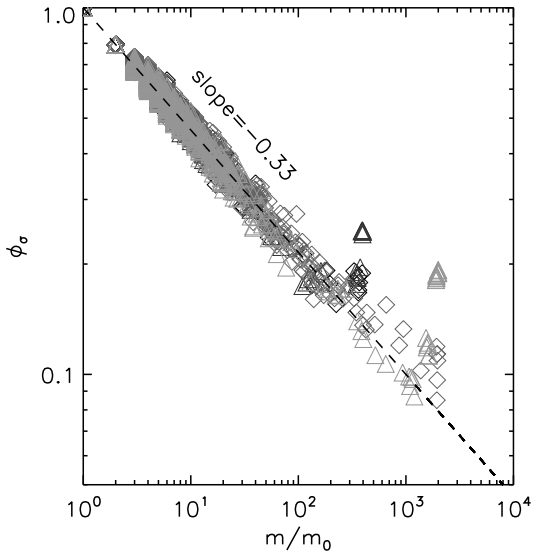

Figure 6.2 — The geometrical filing factor as a function of fragment mass. Many simulations with different sets of parameters are overplotted. The dashed line indicates the least square method fit of the power-law to the small mass fragments.

is the fraction of missing collisions, $f_{\rm miss}$. This number is a correction factor that needs to be applied when the collision cross-section is determined using the outer radius of an aggregate $a_{\rm out}$. The small fragments are described by two quantities: the exponent of the power-law distribution q and the normalized mass of this component $f_{\rm pwl}$. The normalization of this and other quantities are discussed in Sect. 6.3.5.

To fully describe a collision outcome, the recipe also provides the relative change in filling factor, C_ϕ. It describes the compaction or decompaction of aggregates in the large fragment component. Concerning the small fragments that are produced by erosive or fragmenting collisions and constitute the power-law component, a common filling factor can be assigned. The compactness of these particles depends only on mass and is presented in Fig. 6.2, where fragments produced in many simulations are plotted. Almost all particles are located along the power-law with the slope of −0.33. This provides a very easy prescription for the filling factor of small fragments. This dependence indicates a fractal structure (with the fractal dimension of about $D_{\rm f} \approx 2.0$) of aggregates formed in a fragmentation event, since the non-fractal aggregates have filing factor independent of mass.

As shown by Paszun and Dominik (2008a) after reaching the maximum compaction, further increase of the impact energy causes more restructuring and results in a flattening of the produced aggregate. Therefore, very fluffy particles can be produced in collisions of massive aggregates, where the power-law component extends to larger N. This behavior is also observed in Fig. 6.2, where fluffy, small fragments follow the power-law relation, while some large, still

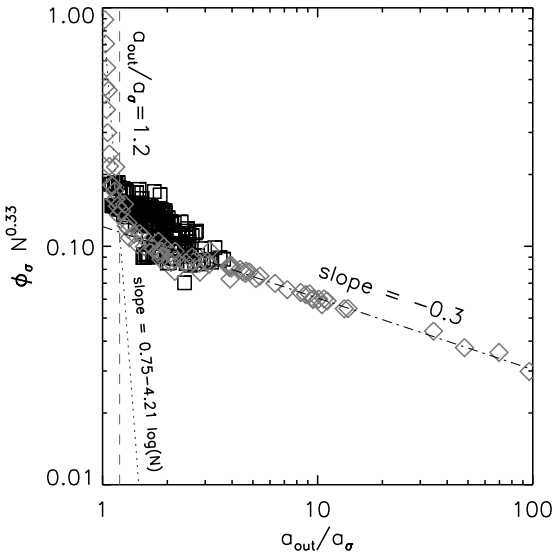

Figure 6.3 — The geometrical filling factor dependence on the ratio of outer to geometrical radii. In this figure we plot $\phi_\sigma N^{0.33}$ to scale the data for aggregates of different mass.

compact particles are above the dashed line.

6.3.4 Relation between $a_{\rm out}$ and a_σ

In this study we distinguish two different radii of an aggregate: the outer radius $a_{\rm out}$ and the projected surface equivalent radius a_σ. The first one is used as a reference of our impact parameter b. The collision offset is limited by the largest impact parameter $b_{\rm max} = a_{\rm out,1} + a_{\rm out,2}$. The cross-section equivalent radius a_σ defines our structural parameter ϕ_σ (see Eq. (6.21)). We determine the relation between the two radii ($a_{\rm out}$ and a_σ) empirically. Both $a_{\rm out}$ and a_σ are determined for many aggregates of various shape and mass. We sample particles with the fractal dimension in the range of $D_{\rm f} = 1 \ldots 3$ and masses from several to a few thousands monomer masses. These aggregates were produced using an algorithm developed by Filippov et al. (2000).

Figure 6.3 shows the filling factor determined for different aggregates versus the ratio of the outer radius over the cross-section equivalent radius. The mass dependence, as determined in Sect. 6.3.3, is shown by plotting $\phi_\sigma\ N^{0.33}$. Diamonds correspond to aggregates of different fractal dimension and mass. Interestingly, the data for all aggregates are very well confined along a single curve. At small ratio of $a_{\rm out}/a_\sigma$ the curve decreases very steeply with increasing $a_{\rm out}/a_\sigma$. This corresponds to compact particles for which $a_{\rm out}/a_\sigma$ does not depend much on filling factor. The line, however, breaks at about $a_{\rm out}/a_\sigma \approx 1.2$ and turns in to a power-law with a slope of -0.3. This shallow relation represents fluffy aggregates that show a large discrepancy between the projected surface

equivalent radius and the outer radius.

In order to provide a simple relation between the two radii, two power-law functions are fitted to the two regimes: compact particles below $a_{\rm out}/a_\sigma = 1.2$ and fluffy aggregates above that limit. These two functions are given by

$$\phi_\sigma^{\rm compact} = \Big(\frac{a_{\rm out}}{a_\sigma}\Big)^{(0.75-4.21\log N)} \tag{6.22a}$$

$$\phi_\sigma^{\rm fluffy} = 1.21\Big(\frac{a_{\rm out}}{a_\sigma}\Big)^{-0.3} N^{-0.33}. \tag{6.22b}$$

To further verify these relations we use particles produced in several simulations performed by Paszun and Dominik (2008a). These aggregates are indicated in Fig. 6.3 by black squares. They show a very similar relation to the one obtained in Eq. (6.22). Points that are slightly shifted above the fitted lines correspond to aggregates that are partly compressed (they did not reach the maximum compaction). Their compact cores are still surrounded by a fluffy exterior that causes a small increase of the ratio of the outer radius over the projected surface equivalent radius $a_{\rm out}/a_\sigma$. This behavior, however, occurs at a relatively small value of $a_{\rm out}/a_\sigma < 2$. At a larger size ratio the filling factor falls back onto the power-law given in Eq. (6.22b).

6.3.5 Parameter space and normalizations

We list the five key parameters that shape the outcome of aggregate collisions:

1. the collision energy, E;
2. the impact parameter, b;
3. the structure of aggregates, ϕ_σ;
4. the mass ratio, N_1/N_2 (local or global influence);
5. monomer properties, $\gamma, \mathcal{E}$.

The influence of the material properties and monomer size can be eliminated by a proper scaling of the energy to the rolling and breaking energies corresponding to the material properties. Thus, we normalize to $E_{\rm roll}$ where it concerns the change in the filling factor, i.e., the C_ϕ parameter reflecting restructuring, and to $E_{\rm br}$ for the other parameters of Table 6.4 that describe the fragmentation behavior.

Another parameter that affects collisions is the mass ratio. This influences mostly the collision outcome in terms of compactness. Impacts of similar size aggregates show compression for small impact parameters ($b \approx 0$) and decompaction for large offsets ($b \sim 1$). On the other hand, impact of a smaller particle onto a larger target results in a similar outcome regardless of the impact parameter. This discrepancy is dealt with by providing two separate sub-recipes:

the local and the global recipe. Collisions of similar mass aggregates result in changes throughout both particles. We refer to this behavior as the *global recipe*. When a mass ratio is smaller than 0.1 the changes become more localized. In this case the energy is concentrated in the region local to the impact area, which may, e.g., result in cratering. This confined behavior is provided in the *local recipe*. The energy in the global recipe is normalized to the total number of monomers, N_{tot}, which represents the extended influence of the collision. However, in the local recipe the energy scales by the reduced number of monomers N_{μ}, which is basically the number of monomers of the smaller collision partner. The dimensionless energy parameter is then defined as

$$\varepsilon = \frac{E}{N_{\mathrm{eff}} E_{\mathrm{crit}}}, \tag{6.23}$$

where E_{crit} and N_{eff} depend on the context: The energy E_{crit} can be either one of E_{br} or E_{roll}, whereas N_{eff} is one of N_{tot} or N_{μ}. The distinction of the two sub-recipes is presented in Sect. 6.3.9.

The remaining three quantities (the normalized energy ε, the impact parameter b, and the filling factor ϕ_{σ}) form the 3D space of input parameters of the recipe. Their influence on the collision outcome is described in § 6.3.7 and 6.3.8, where we first discuss quantities defining the result of an impact. However, before we present the effect of different parameters on a collision outcome in both the local and the global recipes, we discuss impacts in the hit-and-stick energy regime.

6.3.6 Hit and stick

At very low energies ($E \leq 5E_{\mathrm{roll}}$) two aggregates will stick where they meet, without affecting the internal structure of the particles. This is the 'hit-and-stick' regime in which the collisional growth can often be described by fractal laws. Two important limits are cluster-cluster coagulation (CCA) and particle-cluster coagulation (PCA). In the former, two particles of equal size meet, which often leads to very fluffy structures, whereas PCA describes the process in which the projectile particles are small with respect to the target. The filling factor then saturates to a constant value. For example, in the case of monomers, the filling factor will reach the PCA limit of 15% (Kozasa et al. 1992).

In general particles do not merely collide with either similar-size particles or monomers. Every size-ratio is possible and leads to a different change in filling factor. Ormel et al. (2007) provide an analytical expression, based upon fits to collision experiments of Ossenkopf (1993), that give the increase in void space as function of the geometrical volume of the collision partners. Here, the geometrical volume V is the volume that corresponds to the geometrical radius, a_{σ}. Although the expressions of Ormel et al. (2007) are easily convertible into filling factor, we have used additional numerical collision experiments to further constrain these analytical fits. These experiments involved several 'PCA-bombardments' (repeated collisions by monomers) of several aggregates. Using

these data, the adopted expressions in the 'hit-and-stick' regimes are now, in terms of the geometrical volumes ($V_1 > V_2$) of the particles

$$\frac{V_{\rm void}}{V_0} = \max\left[(V_1+V_2)\left(\left(1+\frac{V_2}{V_1}\right)^{3\delta/2-1}-1\right),\ \frac{N_2}{0.087\phi_2}\exp\left[-\left(\frac{15V_2}{V_1}\right)^{0.25}\right]\right]. \quad (6.24)$$

The first term converges to CCA in the limit of $V_2 = V_1$, and is the same as in Ormel et al. (2007). Here, δ is an exponent that reflects the fractal growth in this limit, which, following Ossenkopf (1993), we put at $\delta = 0.95$. The second expression converges to PCA in the limit of $V_2 \ll V_1$. The rationale of providing a second expression is that in the case of $V_2 \ll V_1$ (PCA) the first expression goes to zero very quickly (no voids are added), which is clearly inappropriate as PCA must result in a filling factor of 15%. From the results of our new collision experiments we have altered the dependence of the PCA-part on the volume ratio (V_2/V_1) by inclusion of the exponent of 0.25, which, compared to Ormel et al. (2007), smooths out the fall-off with increasing mass ratio.

In fitting the numerical values in the PCA-part we note, however, that not all numerical experiments could be fitted equally well. In fact, we had to compromise: some experiments were better fit by a more 'smoothed' PCA expression, while others were not. It is probable that for a complete description more parameters are required, e.g., the elongation of the aggregates or their fractal dimension. Here, we have adopted approximate fits that follow the qualitative picture in both the CCA ($V_1 = V_2$) and the PCA ($V_2 \ll V_1$) limit. We note, finally, that 'hit-and-stick' collisions are more prevalent in dense environments like protoplanetary disks, rather than in molecular clouds. In our case, therefore, the hit-and-stick regime is only relevant in the initial stages of coagulation at densities of $n \geq 10^5$ cm^{-3}.

6.3.7 Local recipe

In the local recipe the scaling of the energy parameter ε depends on the quantity it is applied to. When it concerns erosion, it scales with N_μ, the reduced number of monomers of the aggregates, which renders the collision outcome insensitive to the size of the larger aggregate. In the case of restructuring, however, the outcome of a collision depends very much on the size of the large particle. The compaction may be local and moderate, but the affected quantity – the filling factor – describes the particle globally. Thus, C_ϕ is normalized to the total number of aggregates, whereas the other quantities that describe the fragmentation process are normalized to N_μ.

In the local recipe the number of large fragments rarely increases above unity (the exception are 'lucky projectiles' that destroy the central contacts of fluffy aggregates, causing the two sides of the aggregate to become disconnected). This deep penetration of a particle may also result in more severe damage. Fragments produced in a cratering event and on their way out of the eroded aggregate may result in secondary impacts causing stronger erosion. This process is

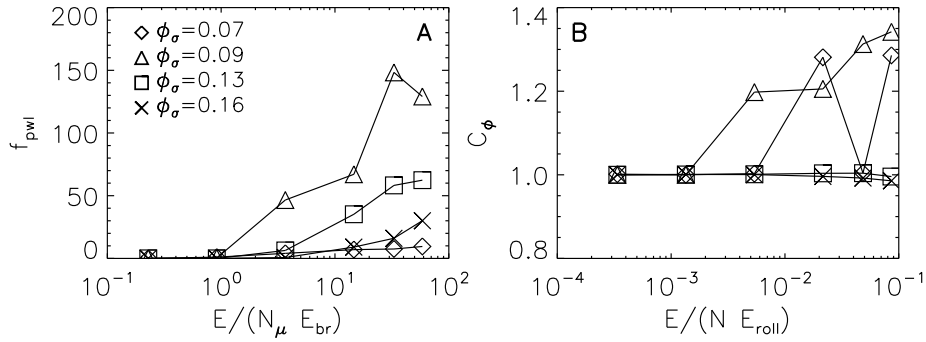

Figure 6.4 — Quantities provided by the local recipe. The left panel shows the mass of small fragments, power-law component, normalized to the reduced mass of the colliding aggregates. The right panel shows the relative change in the geometrical filling factor C_ϕ.

the main cause of fragmentation of large targets, since the energy transfer into the target is not efficient and a large fraction of the kinetic energy is carried away by the ejecta.

Figure 6.4a shows how much of the mass is ejected during collisions at different energies. This mass may exceed the mass of the small projectile by even two orders of magnitude. The collision energy is not transported deep into the target but rather used at the surface to break contacts between monomers. Thus, collisions between particles of different mass result in erosion if sufficient energy is available (a few times $N_\mu E_{\rm br}$).

The local recipe describes cratering that does not fully shatter the target. Erosion events generate a similar distribution, where the slope oscillates between $q = -1.3$ and $q = -2.0$. This is comparable to the slopes obtained for erosive collisions of equal mass projectiles in the global recipe (see Sect. 6.3.8).

Since the influence of the impact is local, the degree of compression is relatively small. However, increasing collision energy results in an increasing degree of compression. The very fluffy and elongated aggregates may break in half causing an artificial increase of the filling factor. This can be observed in Fig. 6.4b for aggregates with $\phi_\sigma^{\rm ini} = 0.07$, where the change in filling factor shows a strong variation for energies above $E = 10^{-2}\ N\ E_{\rm roll}$.

6.3.8 Global recipe

The two key quantities that follow from the recipe are the mass distribution (small and large fragment component) and the change in filling factor of the large fragment component. Figures 6.5a and 6.5b show the number of the largest particles that remain after a collision. The left panel (Fig. 6.5a) shows the result for central impacts of particles of different initial filling factor and at different collision energies. The right panel (Fig. 6.5b) shows the result for collisions at an

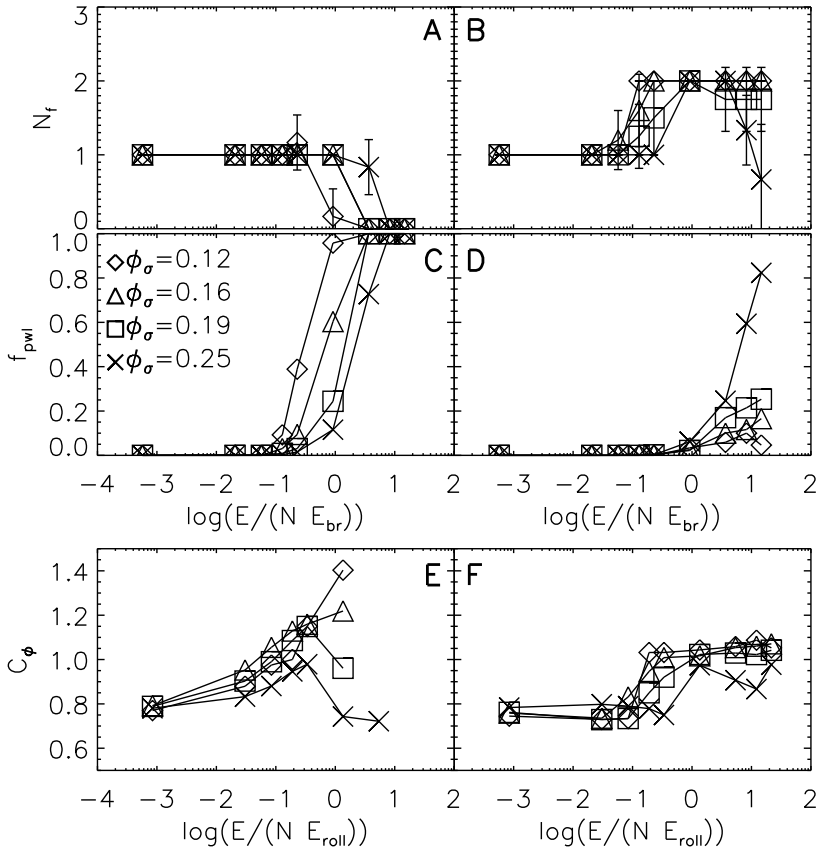

Figure 6.5 — Quantities provided by the global recipe. Left panels correspond to central collisions, while the right panels correspond to off-center collision at impact parameter $b = 0.75$. From top to bottom: Number of large fragments N_f (*A, B*); mass of the small fragments component, M_p, normalized to the total mass of the two aggregates M_{tot} (*C, D*); relative change in the geometrical filling factor $C_\phi = \phi_\sigma/\phi_\sigma^{ini}$ (*E, F*).

impact parameter of $b = 0.75$.

Central impacts at low energy produce one large fragment. An increase of the impact energy results in erosion, where a few small fragments are removed from the surface. In the limit of very high energies ($E > 5NE_{br}$), the interaction leads to catastrophic disruption. Offset collisions, on the other hand, produce two large fragments at high energy collisions. At large impact parameter aggregates interact with their outer parts. This can lead to the formation of only a few contacts that can be easily broken at high impact energies.

The mass distribution of the collision products depends on both energy and

impact parameter. The higher the energy, the smaller the two fragments are. An increase of the impact parameter, however, results in a weaker interaction and an increase of the mass of the fragments. In the limiting case of a grazing collision, two particles are almost unaffected regardless of the impact energy. Collisions between compact aggregates colliding at a very high energy and at a very large impact parameter result in two large fragments, containing in total over 80% of the initial mass.

The number of large fragments N_f is very well defined for central and grazing collisions. In the first case one large fragment remains, while in an off-center impact both collision partners survive. Intermediate impact parameters introduce some ambiguity. Some orientations cause sticking, which leads to one large aggregate, and others produce two large particles. This is reflected in the standard deviation S_f. If all orientations lead to the same outcome, the situation is unambiguous and $S_\mathrm{f} = 0$. However, when the spread in N_f is larger, it defines the probability of a collision to produce one or two fragments.

Figures 6.5c,d show the mass of the power-law component (small fragments). Central collisions result in an equal distribution of energy among the monomers. A collision energy of $3NE_\mathrm{br}$ is sufficient to shatter an aggregate catastrophically. In the case of a fluffy aggregate, the entire particle is destroyed and all fragments belong to the power-law distribution. The most compact aggregate is, however, able to survive these energy inputs. In this case over 70% of the mass is in the power-law component, whereas the rest is in a large fragment. However, the average number of large fragments is below unity and in some cases only the power-law component remains.

An increase of the impact parameter makes the distribution of energy over the aggregate less efficient. This results in a higher threshold for catastrophic destruction: more energy must be provided to completely shatter aggregates. Figure 6.5c,d show that at the energy sufficient to fully shatter compact aggregates at central impact, only 25% of the mass is shattered in an offset collision at impact parameter $b = 0.75$. Fluffy aggregates 'feel' the effect of an increased impact parameter even more, because in this case, the redistribution of the kinetic energy is even weaker. For example, very fluffy aggregates of filling factor $\phi_\sigma = 0.122$ colliding at an impact parameter of $b = 0.75$ produce small fragments which add up to only about 6% of the total mass. The rest of the mass is locked into 2 large fragments.

The degree of damage can also be assessed through the slope of the power-law distribution of small fragments. The steeper the slope, the stronger the damage. Heavy fragmentation produces many small fragments and results in a steepening of the power-law. Although destruction is very strong in the case of a central impact (the slope reaches values of $q = -3.7$ at energy of $> 20NE_\mathrm{br}$), it weakens considerably for offset collisions ($q > -2.0$).

At low energies, the amount of aggregate restructuring, as quantified in the C_ϕ parameter Fig. 6.5e,f, is independent of impact parameter. This is simply because the collision energy is insufficient to cause visible restructuring. Then,

the aggregate volume increases in a hit-and-stick fashion, resulting in a decrease of the filling factor as compared to the initial state of the colliding aggregates.

With increasing collision energy the degree of restructuring is enhanced, and therefore compression occurs. Central impacts strongly affect the filling factor ϕ_σ. Figure 6.5e shows that the compression is maximal at an impact energy of about $E = NE_{\rm roll}$. Those aggregates that are initially compact are difficult to further compress. For static compression, the critical filling factor is $\phi_\sigma = 0.33$ (Blum et al. 2006; Paszun and Dominik 2008b). Any further restructuring can only move monomers sideways, which causes a decrease of the packing density and flattening. Offset collisions, however, lead to much weaker compression as shown in Figure 6.5f. In this case the main reason is that forces acting on monomers in the impacting particles are more tensile, contrary to the compressive forces present in the central collisions. Large offset impacts at velocities above the sticking velocity of about 1 m s^{-1} (Poppe et al. 2000) result in two large fragments with the unaffected filling factor ($C_\phi = 1$).

6.3.9 The recipe's manual

The local and global recipes are generally distinguished by the mass ratio of the colliding aggregates. However, at very high collision energies the results are always well described by the global recipe, even if the mass ratios involved are large. In this case the aggregate is catastrophically disrupted, which, of course, affects the aggregate globally. For example, at a mass ratio of $N_2/N_1 = 0.01$ the velocity required to shatter the target is a 10 times higher than for equal mass aggregates (cf. Eq. (6.19)). At low energies the hit-and-stick recipe will always apply. Figure 5.23 presents the adopted algorithm that provides the distinction between the recipes.

When two aggregates collide at a given impact parameter b and energy E, we first check whether the impact is in the hit-and-stick regime or that energies are above the restructuring limit: $E = 5E_{\rm roll}$. If $E < 5E_{\rm roll}$ no restructuring takes place and the hit-and-stick analytical description discussed above follows. Otherwise, we perform another test. The global influence of the collision occurs if one of two conditions is satisfied:

1. the masses of colliding particles must not differ by more than a factor of 10;

2. the energy must be sufficient to cause global changes to both interacting aggregates.

This latter criterion means that if particles are very different by mass, they will still result in a global change to the properties of the aggregates if the energy is sufficient to break the entire target aggregate. Otherwise, the effect is local and cratering occurs. Equal mass projectiles, however, always affect aggregates globally.

6.4 The Monte Carlo program

In the previous section we have seen that four parameters – the collisional energy E, the filling factor ϕ_σ, the impact parameter b, and the mass ratio in terms of the local and global recipe – determine the outcome of a collision between two aggregates. As the collisional energy depends on mass and the impact parameter is random, we discern two (independent) particle properties: mass and filling factor. From these two quantities all other particle properties are derived. For example, the collisional energy E between two particles depends on the particle masses and the particle's friction times through the relative velocities (see Sect. 6.2), which, in turn, depend on the particle filling factors and masses.

Characterizing particles by only two properties does not fully define their internal structure. For example, we assume that aggregates are spherically symmetric, even though numerical experiments show a distinct elongation (Paszun and Dominik 2006). Still, the collision model contains a significant level of sophistication. The modeling of collisions can be divided in three steps. First, the particle properties (m, ϕ_σ) and the collision properties (Δv) are turned into a collision 'grid point' given by ε, ϕ_σ and b. Then, the outcome of the collision is specified by 6 collision quantities (Table 6.4). Finally, these quantities specify the change to the initial particle properties (m, ϕ_σ) and also describe the properties of the collision fragments.

An important goal of our collision recipe is to make it applicable to a wide range in mass: e.g., it is intended to be applicable to the scales at which the collisional experiments were performed ($\sim 10^3$ monomers) but also to particles of much larger size. This is the rationale behind the scaling of the collision energy to the rolling or the breaking energy, and the distinction between the global and local recipes. We are, therefore, fully equipped to compute the full collisional evolution, even if it takes us well beyond the domain of the numerical experiments, i.e., $N \gg 10^3$. However, we acknowledge that as a consequence of this extrapolation we may not account for physical processes that show up at a different scale; e.g., it may well be the case that particles that have reached a macroscopic proportion will bounce, rather than stick (Langkowski et al. 2008a). We will return to these issues in Sect. 6.6.

The formulation of the collision recipe in terms of the 6 output quantities enables a Monte Carlo (MC) oriented approach to the calculation of the collisional evolution. The advantage of a MC approach is that collisions are modeled individually and therefore have a direct correspondence to the collision model. Furthermore, structural parameters (like ϕ_σ) can be easily included and the collisional outcome can be quantified in detail. Indeed, the outcomes of the collision experiments are quantified by (a change in) 6 critical parameters (see previous section), with the MC program merely sampling the appropriate values (or an interpolation between the appropriate values; see below). We emphasize that our MC model does not represent individual aggregates as in Kempf et al. (1999) but that the particle's structure is merely characterized by two values: the mass of the aggregate or the number of grains, N, and the filling factor ϕ_σ.

In setting up the MC model we have followed previous work of Ormel et al. (2007, 2008a). Furthermore, we implement the new grouping method outlined by Ormel and Spaans (2008). In this method the 1-1 correspondence between a simulation particle and a physical particle is dropped; instead, the simulated particles are represented by *groups* of identical physical particles. Ormel and Spaans (2008) have shown that the method is very well suited to simulate a large dynamic range, which, in the light of the anticipated fragmentation, is exactly what is required. The group's mass is determined by the peak of the $m^2 f(m)$ mass distribution – denoted $m_{\rm p}$ – and particles of smaller mass 'travel' together in groups of total mass $m_{\rm p}$. Grouping entails that a large particle can collide with many small particles simultaneously – a major but necessary approximation of the collision process. This happens when the mass-ratio is less than 1% ($f_\epsilon = 10^{-2}$).

We now continue with an overview of one cycle in the Monte Carlo program, emphasizing in particular the role of the collision recipe and its implementation within the context of the grouping method. Other details concerning the architecture of the MC setup have been discussed in Ormel and Spaans (2008).

6.4.1 One collision cycle

Collision rates

The cycle starts with the calculation (or update) of the collision rates between the groups of the simulation. The individual collision rate between two particles i and j is $C_{ij} = K_{ij}/\mathcal{V}$ (units: s^{-1}), where $\mathcal{V}$ is the simulation volume and K the collision kernel. For grouped collisions C_{ij} is larger because many particles are involved in the collision. The collision kernel K is defined as $K_{ij} = \sigma^{\rm C}_{ij}\Delta v_{ij}$ with $\sigma^{\rm C}_{ij} = \pi a^2_{\rm out}$ the collisional cross section (uncorrected for missing collisions) and Δv_{ij} the average root-mean-square relative velocity. Thus, to calculate the collision rates we need the relative velocities and the relation between the geometrical and the outer radius (Fig. 6.3).

Determination of collision partners

Random numbers determine which two groups collide and the number of particles that are involved from the i and j groups, η_i and η_j. Then, each i-particle collides with η_j/η_i j-particles. The grouping method implicitly assumes that collision rates do not change significantly during the collision process. For erosion or sticking the procedure is appropriate as we only apply grouping when the mass ratio between the i (the large particles) and the j particles (the smaller projectiles) is large. However, in collisions that result in breakage the grouping assumption is potentially problematic, since the particle properties – and hence the collision rates – then clearly change *during* the collisions. Fortunately, breakage is not a frequent occurrence as grouped collisions are only applicable in the local recipe due to the large mass-ratio's. Catastrophic disruptions (shattering)

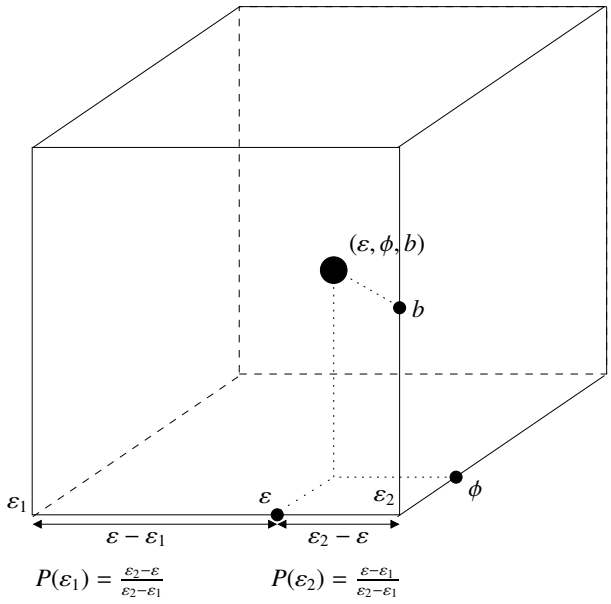

Figure 6.6 — Illustration of the picking of the grid points. The collision takes place at $(\varepsilon, \phi_\sigma, b)$: a point that is generally surrounded by eight grid points (here corresponding to the nodes of the cube). Each node is then assigned a probability inversely proportional to the distance to the grid point. Thus, the probability that the energy parameter $\varepsilon = \varepsilon_1$ is picked (corresponding to four of the eight grid nodes) is $P_1 = (\varepsilon - \varepsilon_1)/(\varepsilon_2 - \varepsilon_1)$. The procedure is identical for the other parameter grid points.

is problematic for the same reasons, because when it occurs, there is no 'large' aggregate left. However, for energetic reasons we expect that shattering occurs mainly when two equal-size particles are involved, for which the global recipe would apply (and no grouping). In the following we continue with a collision of $\eta_t = \eta_j/\eta_i$ j-particles colliding with a single i-particle.

Interpolation of data cubes

When the collision is in the 'hit-and-stick' regime the properties of the new particles are easily found by adding the masses of the j-particles to the i-particle and calculating their filling factor using Eq. (6.24). In the following we will outline only the changes in either the local or global recipe. The collision is then characterized by three parameters: normalized collision energy ε, filling factor ϕ_σ and impact parameters b. The energy parameter ε is different for the local and the global recipe and is normalized with respect to the breaking energy except in the case of the C_ϕ quantities where it is normalized to the rolling energy (Sect. 6.3.5). These three parameters constitute an arbitrary point in the 3D $(\varepsilon, \phi_\sigma, b)$-space, and will in general be 'surrounded' by 8 grid points (k) which correspond to the parameters at which results from the collision experiments are available. We next distribute the η_t collisions over the grid point in which the weight of a grid point is inversely proportional to the 'distance' to $(\varepsilon, \phi_\sigma, b)$ as explained in Fig. 6.6. Taking account of the collisions that result in a miss, we have

$$\eta_t = \eta_{\text{miss}} + \sum_k \eta_{k\cdot}, \qquad \eta_{\text{miss}} = \sum_k \eta_{\text{miss},k}, \tag{6.25}$$

where $\eta_{\mathrm{miss},k} = [\eta_t P_k f_{\mathrm{miss},k}]$ denotes the number of collisions at the grid point resulting in a miss. Here, P_k denotes the weight of the grid point, f_{miss} the fraction of missed collisions at the grid point and the brackets indicates this number is rounded to integer values. Similarly, the number of 'hits' at a grid point is given by $\eta_k \simeq \eta_t P_k(1 - f_{\mathrm{miss},k})$. Not all of these grid points have to be occupied (i.e., η_k can be zero). In the special case without grouping $\eta_t = 1$ and only one grid point at most is occupied.

We continue here to outline the general case of multiple occupied grid points. First, we consider the mass that is eroded, given by the $f_{\mathrm{pwl},k}$ quantities. The mass eroded at one grid point per collision is given by $M_{\mathrm{pwl},k} = f_{\mathrm{pwl},k}(m_i + m_j)$. Then, the total mass eroded by the group collision is

$$M_{\mathrm{pwl}} = \sum_k M_{\mathrm{pwl},k}\eta_k. \tag{6.26}$$

If this is more than m_i, then clearly there is no large fragment component.[3] Otherwise, the mass of the large fragment component is $M_{\mathrm{large}} = m_i + (\eta_t - \eta_{\mathrm{miss}})m_j - M_{\mathrm{pwl}}$. Each $M_{\mathrm{pwl},k}$ quantity is distributed as a power-law with the exponent provided by the slope q_k of the grid point (see below). Concerning the large-fragment component, there is a probability that it will break, given by the $N_{\mathrm{f},k}$ and $S_{\mathrm{f},k}$ quantities. As argued before, breakage within the context of the grouping algorithm cannot be consistently modeled. Notwithstanding these concerns, we choose to implement it in the grouping method. Because its probability is small, we assume it happens at most only once during the group collision. The probability that it occurs is then

$$P_2 = 1 - \prod_k (1 - P_{2,k})^{\eta_k}, \tag{6.27}$$

where $P_{2,k}$ is the probability that breakage occurs at a grid point and follows from the S_{f} and N_{f} quantities. If breakage occurs, the masses M_{pwl} are removed first and we divide the remaining mass M_{large} in two.

The last quantity to determine is the change in the filling factor of the large aggregate, denoted previously by the C_ϕ parameter. Like Eq. (6.27) we multiply the changes in C_ϕ at the individual grid nodes,

$$C_\phi = \prod_k C_{\phi,k}^{\eta_k}, \tag{6.28}$$

and $\phi_{\sigma,\mathrm{large}} = C_\phi \langle \phi_\sigma \rangle_m$. This completes the implementation of the collisional outcome within the framework of the grouping mechanism. That is, we have the masses and the new ϕ_σ-values of the large fragment component(s), and have computed the distribution of the power-law component in terms of mass. Note again that all these results are *per i*-particle, and that the multiplicity of the results is η_i.

[3] Recall that in grouped collisions ($\eta_{\mathrm{t}} > 1$) this implies that the grouping method is not fully accurate as the change in mass is of the order of the mass itself; but the procedure is always fine if $\eta_{\mathrm{t}} = 1$.

Picking of the power-law component masses

The final part of the MC cycle is to pick particles according to the power-law distribution, under the constraints of a total mass $M_{\rm pow}$ and slope q. (If $M_{\rm pow} = 0$ there is of course no mass to distribute.) This must be done at each grid point k, because the slope q_k in general is different at each grid point. The mass $M_{\rm pow}$ is the mass that goes into fragmentation at the grid point k, $M_{{\rm pwl},k}$, multiplied by η_k and η_i (the collision multiplicity). The general formula for picking the mass of the fragments is

$$m_i = \left[1 + \bar{r}(m_{\rm rem}^{1+q} - 1)\right]^{\frac{1}{1+q}} , \tag{6.29}$$

where $m_{\rm rem}$ is the maximum mass of the distribution (this decreases at every step and should from the definitions above be no more than 25% of the total mass) and $\bar{r}$ a random number between 0 and 1. Equation (6.29) is obtained from

$$\bar{r} = \int_1^m {\rm d}x\, x^q \Big/ \int_1^{m_{\rm rem}} {\rm d}x\, x^q \ . \tag{6.30}$$

In the MC program the number of *distinct* fragments that can be produced is limited to a few per grid point. This is to prevent an influx of a very large number of species (non-identical particles; in this case, particles of different mass), which would lead to severe computational problems, filling-up the state vector array (see below). Therefore, if the same mass m_i is picked again it is considered to be the same species, and the multiplicity of this species is increased by one. After we have obtained a maximum of $\eta_{\rm dis}$ *distinct* species, we redistribute the mass $M_{\rm pow}$ over the species. In this way the fragment distribution is only sampled at a few discrete points.

Merging/Duplication

The final part of the MC program consist of an inventory, and possible adjustment, of the amount of groups and species ($N_{\rm s}$) present in the program. To combine a sufficiently high resolution with an efficient computation in terms of speed is one of the virtues of the grouping method. One key parameter, determining the resolution of the simulation, is the $N_{\rm s}^*$ parameter (the target number of species in a simulation). In order to obtain a sufficient resolution we require that a total mass of $\sim m_{\rm p} N_{\rm s}^*$ is present in the simulation. Particles are *duplicated* to fulfill this criterion, adding mass to the system. To prevent a pileup of species we have adopted the 'equal mass method' as described in Ormel and Spaans (2008). However, we found that due to the fragmentation many species were created at any rate | too many, in fact ($N_{\rm s} > N_{\rm s}^*$) which would severely affect the efficiency of the program. Therefore, if $N_{\rm s} = 2N_{\rm s}^*$ we used the 'merging algorithm,' in which neighboring species are combined into one species, averaging over their (structural) parameters. This significantly improved the efficiency (i.e., speed) of the simulation, although the many fragments created by the collisions (all contributing to a higher $N_{\rm s}$) can be regarded as a redundancy, because

Table 6.5 — Overview of the model runs. (1) Model number. (2) Number density of the gas. (3) Collision type, describing material parameters and collision setup. Here 'ice' refers to ice-coated silicates of bulk density that is the same to that of silicates, ρ_0 = 2.65 g cm^{-3}, and material parameters γ = 370 erg cm^{-2} and $\mathcal{E}^\star$ = 3.7×10^{10} dyn cm^{-2}. For bare silicates, γ = 25 erg cm^{-2} and $\mathcal{E}^\star$ = 2.8×10^{11}. (4) Monomer radius. (5) Figure reference. *Notes:* [a]the standard model; [b]filling factor of particles restricted to a minimum of 33%. [c]central impact collisions only (b = 0).

id	Density n [cm^{-3}]	Type	Grain size a_0 [μm]	Figure reference
(1)	(2)	(3)	(4)	(5)
1	10^3	ice	0.1	
2	10^4	silicates	0.1	Fig. 6.12
3	10^4	ice	0.1	Fig. 6.12
4	10^5	silicates	0.1	Fig. 6.12
5	10^5	silicates	1	
6[a]	10^5	ice	0.1	Figs. 6.7, 6.9, 6.8
7	10^5	ice	1	Fig. 6.13
8	10^5	ice	0.03	Fig. 6.13
9	10^5	ice, compact [b]	0.1	Fig. 6.10
10	10^5	ice, head-on [c]	0.1	Figs. 6.9, 6.10
11	10^6	silicates	0.1	Fig. 6.12
12	10^6	ice	0.1	Fig. 6.12
13	10^7	ice	0.1	

it requires a lot of subsequent regrouping. The alternative would be to produce only 1 new species per collision event (Zsom and Dullemond 2008); here, we prefer to stick with a more detailed representation of each collision event by creating many particles, but we acknowledge that this amount of detail is to some extent lost by the subsequent *merging*.

6.5 Results

All requirements to calculate the collisional evolution of dust grains are now in place. In Sect. 6.4 we have discussed how the collision model of Sect. 6.3 is treated in the context of a MC model. We have calculated a large set of models varying the relevant parameters: the density, grain size and material properties. We investigated grains consisting of silicates, and silicates with ice mantles. These properties of the simulation runs are summarized in Table 6.5. Only static models are considered, characterized by a constant density. To obtain a measure of the influence of the density on the coagulation process – timescales and amount of growth – a large range in density is considered. The coagulation is followed for 10^7 yr in most of the models, unless a steady state has clearly appeared before this time. Other parameters that affect the coagulation process

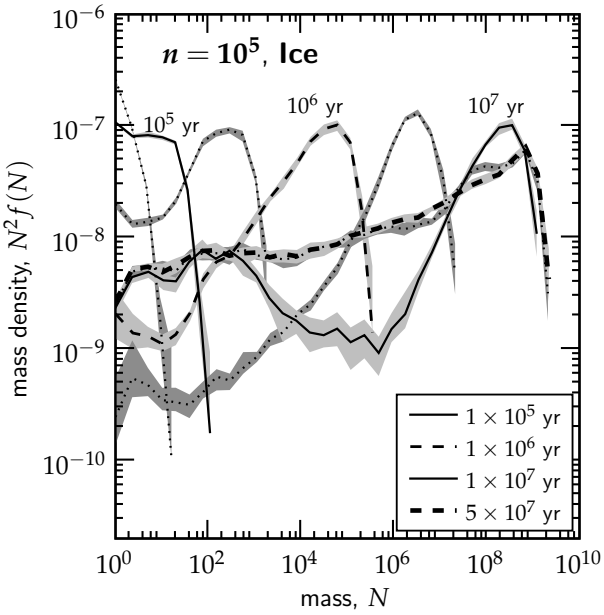

Figure 6.7 — Mass distribution of the standard model ($n = 10^5$ cm^{-3}, $a_0 = 10^{-5}$ cm, ice-coated silicates) at several times during its collisional evolution, until $t = 5 \times 10^7$ yr. The distribution is plotted at times of 10^i yr (solid lines, except for the 10^6 yr curve, which is plotted with a dashed line) and 3×10^i yr (all dotted lines), starting at $t = 3 \times 10^4$ yr. The grey shading denotes the spread in 10 runs. Mass is given in units of monomers. The final curve (thick dashed line) corresponds to 5×10^7 yr and overlaps the 3×10^7 yr curve almost everywhere, indicating that steady-state has been reached.

but which are fixed here – i.e., $T = 10$ K, $\mu = 2.34$, etc. – are discussed in Sect. 6.2.

We continue in Sect. 6.5.1 with the analysis of the standard model ($n = 10^5$ cm^{-3}, $a_0 = 0.1$ μm, ice-coated silicates). In Sect. 6.5.2, the results of our parameter study are presented.

6.5.1 The standard model

Figure 6.7 shows the progression of the collisional evolution of ice-coated silicates at a density of $n = 10^5$ cm^{-3} (the standard model). Each curve shows the average of 10 simulations, where the grey shading denotes the 1 σ spread in the simulations. At $t = 0$ the distribution starts out monodisperse at size $N = 1$. Here, N denotes the number of monomers in an aggregate and is a dimensionless measure of the mass. The distribution function $f(N)$ gives the number of aggregates per unit volume such that $f(N)\mathrm{d}N$ is the number density of particles in a mass interval $[N, N + \mathrm{d}N]$. Thus, at $t = 0$ the initial distribution has a number density of $f(0, t = 0) = n\mu m_\mathrm{H}/\mathcal{R}_\mathrm{gd} m_0 = 3.5 \times 10^{-7}$ cm^{-3} in the case of $n = 10^5$ cm^{-3} and $a_0 = 0.1$ μm. On the y-axis $N^2 f(N)$ is plotted at several distinct times during the collisional evolution, which shows the mass of the distribution in a logarithmic interval. The mass where $N^2 f(N)$ peaks in Fig. 6.7 is denoted the mass peak: it corresponds to the particles in which most of the mass is contained. The peak of the distribution curves stays on roughly the same level during its evolution, reflecting conservation of mass density.

After $t = 10^5$ yr (first solid line) a second mass peak has appeared at $N = 10$

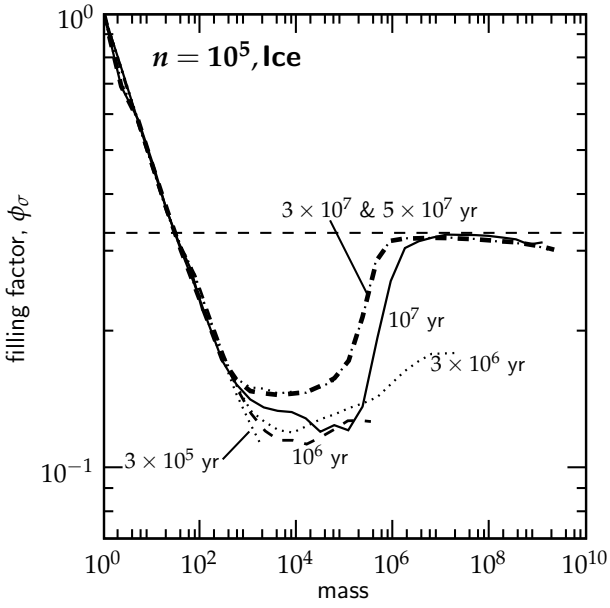

Figure 6.8 — The distribution of the filling factor, ϕ_σ, in the standard model, plotted at various times. In the fractal regime, the porosity decreases as a power-law, $\phi \simeq N^{-0.3}$. Compaction is most severe for the more massive particles, where the filling factor reaches the maximum of 33%. Only mean quantities are shown, not the spread in ϕ_σ.

that separates itself from the initial distribution. The peak at $N = 1$ is a remnant of the compact ($\phi_\sigma = 1$) size and smaller collisional cross-section of monomers compared with dimers, trimers, etc. – not by fragmentation. Furthermore, the high collisional cross section of, e.g., dimers is somewhat overestimated, being the consequence of the adopted power-law fit between the geometrical and collisional cross section (Fig. 6.3). These effects are modest and do not affect the result of the simulation. Meanwhile, the porosity of the aggregates steadily increases, initially by hit-and-stick collisions but after $\sim 10^5$ yr mostly through low-energy collisions between equal-size particles (global recipe) that do not visible compress the aggregate. In Fig. 6.8 the porosity distribution is shown at several times during the collisional evolution. Initially, due to low-energy collisions the filling factor decreases as a power-law with exponent $\simeq 0.3$, $\phi_\sigma \simeq N^{-0.3}$. This trend ends after $N \sim 10^4$, at which collisions have become sufficiently energetic for compaction to halt the fractal growth. The filling factor then flattens out and increases only slowly. At $t = 3 \times 10^6$ yr the $N \sim 10^7$ particles are still quite porous.

After $t = 3 \times 10^6$ yr collisions have become sufficiently energetic for particles to start fragmenting, significantly changing the appearance of the distribution. Slowly, particles at low mass are replenished and growth decelerates. When inquiring the statistics underlying the fragmenting collisions, we find that collisions that result in fragmentation are mostly of a (very) modest erosive nature, in which only a few percent of the mass of the large aggregate is removed. Therefore, when erosion first appears, growth is not immediately halted, but it is effective in replenishing the particles at low-N. With time, however, the stationary point is unquestionably reached as collisions will eventually enter a regime

in which there is no net growth. The collisional evolution does never proceed to a stage in which shattering collisions dominate the fragmentation.

The collision experiment is continued beyond 10^7 yr, until the point where a steady-state has been reached. At 10^7 yr the largest particles have reached the upper limit of 33% for the filling factor. The compaction increases the collision velocities between the particles and therefore enhances the fragmentation. At 3×10^7 yr the distribution curve has flattened-out significantly. The final curve ($t = 5 \times 10^7$ yr) mostly overlaps the 3×10^7 curve (both in Figs. 6.7 and 6.8) and therefore indicates that steady-state has been reached. At this stage most of the mass resides in ~100 μm grains. However, small particles, due to the fragmentation, are again dominant by number.

The transition towards a flat mass spectrum is consistent with a scenario in which mass is injected at $N = 1$, and then 'flows' to large-N at which it is fragmented, or, in this case, eroded. Indeed, the erosive nature of fragmenting collisions produces mostly low-N particles. The change in the shape of the mass function with time also provides a clue why the curves in Fig. 6.8 do not overlap in the intermediate-N region. At times before 10^7 yr, the point where the curves terminate correspond to the most massive particles in the distribution. These are quite rare and therefore preferentially collide with particles of lower mass, which suppresses the collisional energies due to the mass-ratios. When the distribution has flattened out, however, equal-mass collisions are more important and the higher energies involved cause compaction to occur at lower N.

Compact and head-on coagulation

To further understand the influence of the porosity on the collisional evolution we plot in Fig. 6.9 the progression of a few key quantities as function of time: the mean size $\langle a \rangle$, the mass-average size $\langle a \rangle_m$, and the mass-average filling factor $\langle \phi_\sigma \rangle_m$ of the distribution. Here, mass-average quantities are obtained by weighing the particles of the MC program by mass; e.g., the mass-weighted size is defined as

$$\langle a \rangle_m = \frac{\sum_i m_i a_i}{\sum_i m_i}. \tag{6.31}$$

The weighing by mass has the effect that only the massive particles contribute – provided these particles dominate the mass peak, which is mostly the case when the distribution is evolved. On the other hand, in a regular average all particles contribute equally, meaning that this quantity is particularly affected by the particles that dominate the number distribution. Thus, as particles start out monodisperse, $\langle a \rangle_m = \langle a \rangle$. However, over time $\langle a \rangle_m$ starts to move away from the mean size of the distribution, meaning that most of the mass becomes locked up in large particles but that the small particles still dominate the number distribution. This picture is consistent with the distribution plots in Fig. 6.7.

How important is the adopted collision recipe in shaping the distribution? To assess this question we additionally ran simulations in which the collision recipe is varied with respect to the standard model. The distribution functions

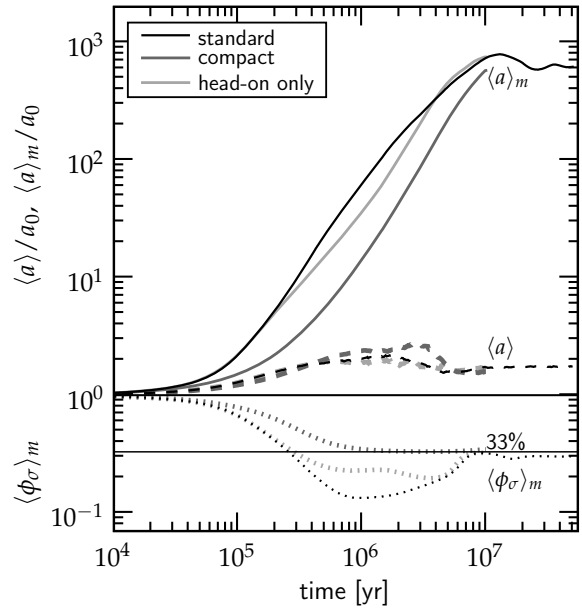

Figure 6.9 — (*black curves*) The temporal evolution of the mean size $\langle a \rangle$ (*dashed curve*), the mass-weighted size $\langle a \rangle_m$ (*dotted curve*) and the mass-weighted filling factor, $\langle \phi_\sigma \rangle_m$ (*solid curve*) of the distribution for the standard model. (*dark grey curves*) Compact model, in which the filling factor stays above 33%. (*light grey curves*) The standard model restricted to head-on collisions only.

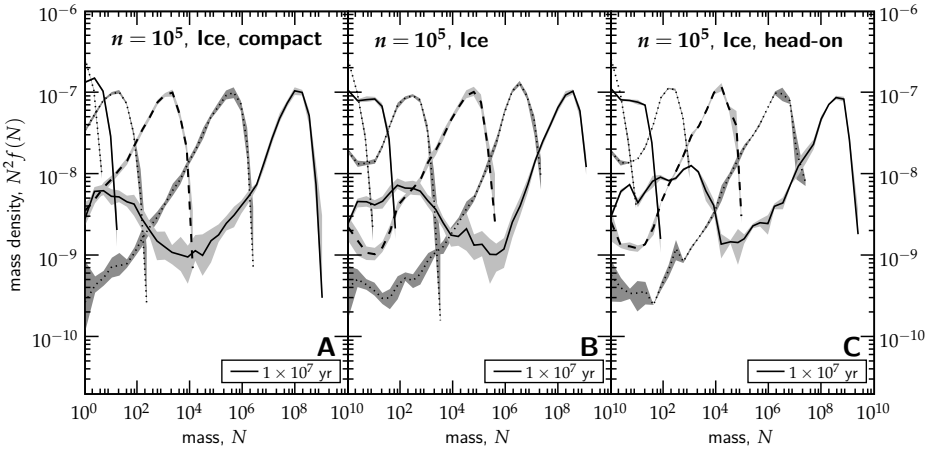

Figure 6.10 — Plots that test the influence of the collision recipe on the evolution of the size distribution for the standard model where ice-coated silicates are treated. (*a*) compact coagulation, in which the filling factor is restricted to a lower limit of 33%. (*b*) the standard model, shown for comparison. (*c*) head-on collisions only, where the impact parameter is fixed at $b = 0$ for every collision. The evolution extends until $t = 10^7$ yr.

of these runs are presented in Fig. 6.10, whereas Fig. 6.9 also shows the computed statistical quantities (until $t = 10^7$ yr). In the case of compact coagulation the filling factor of the particles was restricted to a minimum of 33% (small particles like monomers can still have higher filling factors). Clearly, the results show that the initial stages of the growth is much faster for porous aggregates (cf. Fig. 6.10a and Fig. 6.10b). This can be understood by considering the dependence on filling factor of the friction time and the cross-section

$$\tau_\mathrm{f} \propto N^{1/3}\phi_\sigma^{2/3}; \tag{6.32a}$$

$$\sigma \propto N^{2/3}\phi_\sigma^{-2/3}, \tag{6.32b}$$

where we substituted for simplicity the geometrical cross section σ_ϕ for the collisional cross-section σ_ϕ^C. Because velocities depend on the square-root of the friction time, the collision rate, $K = \sigma\Delta v$, has a $-1/3$ dependence on filling factor, $K \propto N^{5/6}\phi_\sigma^{-1/3}$. Therefore, the collision rate is increased if filling factors decrease. Porous aggregation, then, shortens the growth timescale.

Figure 6.10c presents the results of the standard model in which collisions are restricted to take place head-on, an assumption that is frequently employed in collision studies. That is, except for the missing collision probability (f_miss), the collision parameters are obtained exclusively from the $b = 0$ entry. In this way we can assess the importance of offset collisions. The temporal evolution of the head-on only model is also given in Fig. 6.9 by the light-grey curves. It can be seen that the particles are generally less porous than in the standard model. This follows also from the recipe, see Fig. 6.5: at intermediate energies ($E/N_\mathrm{tot}E_\mathrm{roll} \sim 1$) central collisions are much more effective in compacting than offset collisions. For these reasons, also, growth in the standard model is somewhat faster during the early stages. However, at later times the differences between Fig. 6.10b and Fig. 6.10c become relatively minor, indicating that head-on or offset collisions do not result in a very different fragmentation behavior.

A simple analytical model

Despite the complexity of the recipe, it is instructive to approximate the initial collisional evolution with a simple analytical model. From the preceding discussion it is clear that the evolution of the filling factor drives the growth, as this quantity implicitly determines the velocity structure and the collision timescales. Continuing from Eq. (6.32) we can write

$$\Delta v \propto \tau_\mathrm{f}^{1/2} \propto N^{1/6}\phi_\sigma^{1/3}; \tag{6.33a}$$

$$t_\mathrm{coll} = (n_\mathrm{d}\Delta v\sigma)^{-1} \propto N^{1/6}\phi_\sigma^{1/3}, \tag{6.33b}$$

where the monodisperse assumption $n_\mathrm{d} \propto N^{-1}$ has been applied. As explained in Sect. 6.2.2 the expression $\Delta v \propto \tau_\mathrm{f}^{1/2}$ holds only for the square-root part of the turbulence, but this is fully appropriate for the molecular cloud environment.

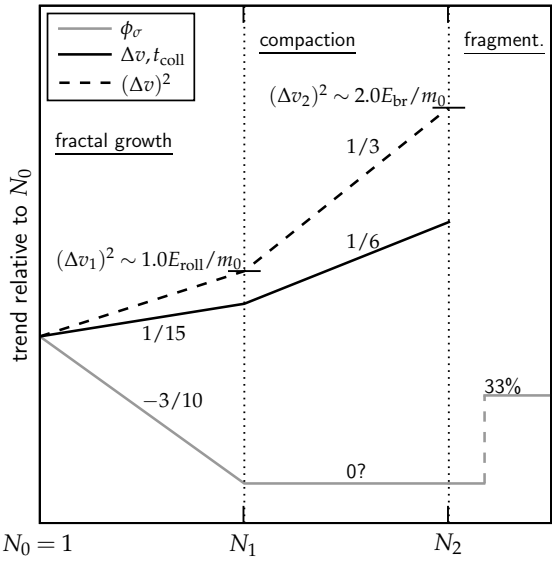

Figure 6.11 — (*grey line*) A simplified model for the behavior of the filling factor with growth. Initially, if Δv_0 is sufficiently low, the porosity decreases (fractal growth regime). This phase is followed by a "status quo" phase where filling factors will be approximately constant. The first compaction event is reached when velocities reach Δv_1 and fragmentation sets in when relative velocities exceeds Δv_2. (*solid line*) Trend of the collision velocity and collision timescale. (*dashed line*) Trend of $(\Delta v)^2$. The numbers denote the power-law exponents.

Then, relative velocities and collision timescales have the same dependence on N and ϕ_σ. Concerning ϕ_σ Fig. 6.8 suggest that the initial evolution of ϕ_σ can be divided in two regimes, where the transition point occurs at a mass N_1. Initially ($N < N_1$), the filling factor is in the fractal regime, which can be well approximated by a power-law, $\phi_\sigma \simeq N^{-3/10}$. We refer to this regime as the fractal regime, because it includes hit-and-stick collisions (no restructuring) as well as collisions for which $E > 5E_{\rm roll}$ but which do not lead to *visible* restructuring, i.e., only a small fraction of the grains take part in the restructuring. For $N > N_1$ the filling factor starts to flatten-out. It is difficult to assign a trend for ϕ_σ in the subsequent evolution. Following Fig. 6.8 we may assume that initially ϕ stays approximately constant for several orders of magnitude in N, but at some point it will quickly assume its compact value of 33%. Here, we assume that the collapse of the porous structure takes place *after* the point where the first erosive collisions occurs, at $N = N_2$. A sketch of the adopted porosity structure and the resulting scaling of velocities and timescales is presented in Fig. 6.11.

From the collision recipe (Sect. 6.3.2) we can identify the critical energies where visible compaction and fragmentation occur. In the first case, the global recipe applies and Fig. 6.5 shows that the transition to compaction ($C_\phi > 1$) corresponds to a normalized energy of $\varepsilon_{\rm roll} = E/NE_{\rm roll} \simeq 0.2$. On the other hand the simulations clearly show that small particles are replenished by fragmentation in the form of erosive collisions. From Fig. 6.4 we can assign an energy threshold of $\varepsilon_{\rm br} = E/N_\mu E_{\rm br} \simeq 1.0$. Working out these expressions and using a typical mass ratio of 3 for the global recipe ($N_\mu = N/6$), we find that these energy criteria corresponds to relative velocities of $(\Delta v_1)^2 \simeq 1.0 E_{\rm roll}/m_0$ and $(\Delta v_2)^2 \simeq 2.0 E_{\rm br}/m_0$, respectively. These energy thresholds are also indicated in Fig. 6.11.

From these expressions and the initial expressions for the relative velocity and the collision timescale (Eqs. (6.15) and (6.16)), the turn-over points N_1 and N_2 can be calculated. We assume that $\Delta v_0 < \Delta v_1$ such that a fractal growth regime exist. Then, the first transition point is reached at a mass

$$N_1 \sim \left(\frac{\Delta v_1}{\Delta v_0}\right)^{15} = \left(\frac{1.0 E_{\rm roll}}{m_0(\Delta v_0)^2}\right)^{7.5} = 2{\times}10^3 \left(\frac{n}{10^5\ {\rm cm}^{-3}}\right)^{3.75} \left(\frac{\gamma}{370\ {\rm erg\ cm}^{-2}}\right)^{7.5} \left(\frac{a_0}{0.1\ \mu{\rm m}}\right)^{-22.5}. \tag{6.34}$$

Unfortunately, the high powers make the numeric evaluation rather unstable. In our simulations we find that $N_1 \sim 10^4$. Subsequently, we can write for the second transition point, the onset of fragmentation, N_2,

$$\frac{N_2}{N_1} \sim \left(\frac{\Delta v_2}{\Delta v_1}\right)^{6} = \left(2.0\frac{E_{\rm br}}{E_{\rm roll}}\right)^{3} = 5{\times}10^4 \left(\frac{\gamma}{370\ {\rm erg\ cm}^{-2}}\right)\left(\frac{a_0}{0.1\ \mu{\rm m}}\right)\left(\frac{\mathcal{E}^\star}{3.7\times10^{10}\ {\rm dyn\ cm}^{-2}}\right)^{-2}, \tag{6.35}$$

which corresponds also well to the results from the simulation for which $N_2 \sim 10^8$. In our simulations the *first* fragmentation involves particles that are still relatively porous, such that the assumption in Fig. 6.11 about the porosity of the N_2-particles is justified. However, once steady-state has been reached, particles of $N_2 \sim 10^8$ will have a 33% filling factor (see Fig. 6.8).

Equations (6.34) and (6.35) also provide a clue how the collisional evolution will behave under different conditions. First, Eq. (6.35) shows that the ratio N_2/N_1 depends on the critical energies only, and therefore that this ratio should stay the same for the same material properties. The $n^{3.75}$ dependence on gas density in Equation (6.34) indicates that the transition points shift $\simeq$1 magnitude in size when the gas density increases by a factor of 10. Even more critical is the dependence on grain size, a_0. This follows directly from the requirement that for visible restructuring *all* grains have to participate. A smaller grain size makes this requirement harder to obtain. Together with the lower initial velocity (lower Δv_0) and the extremely shallow way relative velocities evolve in the fractal regime, aggregates are expected to become very large when $a_0 < 0.1\ \mu$m.

Using a monodisperse model we can also obtain the timescales t_1, t_2 at which these transition points are reached. Starting from the expression

$$\frac{{\rm d}N}{{\rm d}t} = \frac{N}{t_{\rm coll}}, \tag{6.36}$$

the collision time $t_{\rm coll}$ is approximated by a power-law assumption, $t_{\rm coll} = t_{{\rm coll},i}(N/N_i)^\lambda$. Here, $t_{{\rm coll},i}$ is the collision timescale at the point N_i. Specifically, $t_{\rm coll,0}$ is the initial collision timescale (Eq. (6.16)). Straightforward integration then leads to

$$\frac{t - t_i}{t_{{\rm coll},i}} = \frac{1}{\lambda}\left[\left(\frac{N}{N_i}\right)^\lambda - 1\right]; \qquad (N > N_i). \tag{6.37}$$

For $i = 0$, $\lambda = 1/15$ and $N_1/N_0 \sim 10^4$ it results that the fractal growth stages takes ~12 initial collision timescales, or $\sim 10^6$ yr (cf. ~$6{\times}10^5$ yr in the simulation). In the

second regime $\lambda = 1/6$, $t_{\rm coll,1} \simeq 2t_{\rm coll,0}$ and taking $N_2/N_1 = 10^4$ it follows that $t_2 - t_1 \sim 40t_{\rm coll,0}$. Altogether, we may expect that the first fragmentation event takes place after ~50 collision timescales. The simulation shows that in the standard model ~65 initial collision times are required. Because the collision timescale only slowly changes, we may expect the calculated timescales present a general picture, i.e., both compaction and fragmentation take place in a $\sim 10 - 100t_{\rm coll,0}$ interval.

6.5.2 Parameter study

In Fig. 6.12 the collisional evolution of silicates and ice-coated particles are contrasted at densities of $n = 10^4, 10^5$ and 10^6 cm^{-3}. Simulations run until a time of 10^7 yr, except for Fig. 6.12c where a steady state has been reached before. The reason to stop the calculation, then, is that in steady-state the average inter-collision timesteps will be constant, whereas in the preceding 'pure-growth' scenario, the inter-collision time increases. The linear behavior makes it computationally intensive to further evolve the distribution for similar timescales. Again, distributions are plotted at fixed logarithmic timesteps between $t = 3 \times 10^4$ yr and $t = 10^7$ yr, where the curves correspond to the same times as in Fig. 6.7.

Figure 6.12a-c show the collisional evolution of silicates at various densities. In most of the models fragmentation is important from the earliest timescales on. This is of course a consequence of the much lower breaking energy $E_{\rm br}$ that silicate monomers have compared with ice-coated silicates. As a result, in terms of size the growth is very modest: only a factor of 10 in the $n = 10^6$ cm^{-3} model, whereas at even lower densities most of the mass stays in monomers. For the same reason, silicates reach steady state much quicker than ice-coated particles, on a timescale of 10^6 yr.

This situation becomes very different, however, if the silicates are coated with ice (Fig. 6.12d-f). Much more energetic collisions are then required to break aggregates and aggregates grow large indeed. In all cases the qualitative picture reflects that of our standard model, discussed in Sect. 6.5.1: porous growth in the initial stages, followed by compaction and fragmentation in the form of erosion. The evolution towards steady-state is a rather prolonged process, and is only complete within $t = 10^7$ yr in Fig. 6.12f. Again, steady state is characterized by a rather flat mass spectrum. In the low density model of Fig. 6.12d fragmentation does not occur within 10^7 yr.

In Fig. 6.13 the collisional evolution is contrasted at three different values for the monomer size: $a_0 = 300$ Å (Fig. 6.13a), 0.1 μm (the standard model, Fig. 6.13b), and $a_0 = 1$ μm (Fig. 6.13c). To obtain a good comparison, Fig. 6.13 uses physical units (grams) for the mass of the aggregates, rather than the dimensionless number of monomers, N. The effects of varying a_0 are twofold. First, as we have seen above, the length of the fractal growth phase (no compaction or fragmentation) is very sensitive to a_0. Second, the monomer size a_0 directly reflects the amount of energy dissipation of the material. In the litera-

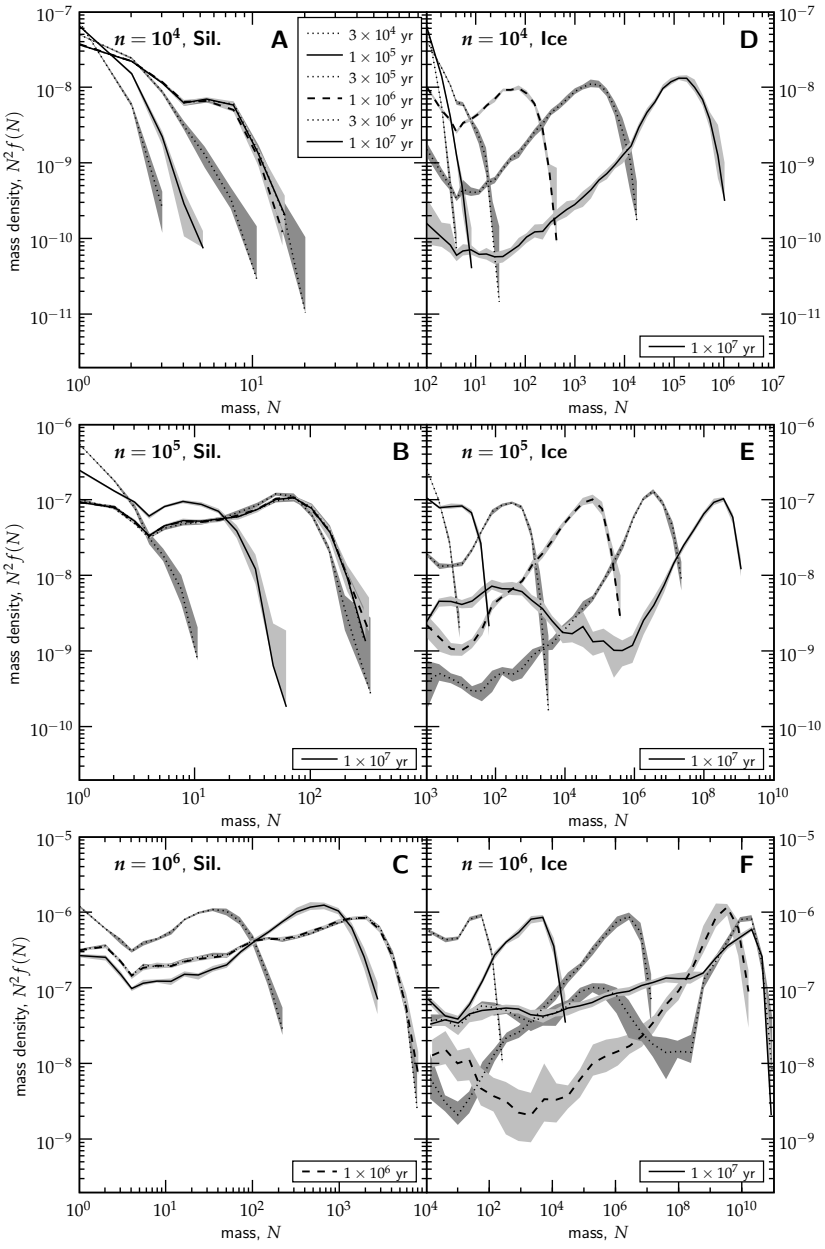

Figure 6.12 — Distribution plots corresponding to the collisional evolution of silicates (*left* panels) and ice-coated silicates (*right* panels) at densities of $n = 10^4, 10^5$ and 10^6 cm^{-3} until $t = 10^7$ yr. For the silicates a steady-state between coagulation and fragmentation is quickly established on timescales of $\sim 10^6$ yr, whereas ice-coated silicates grow much larger before fragmentation kicks in. The initial distribution is monodisperse at $a_0 = 10^{-5}$ cm. Note the different x-scaling.

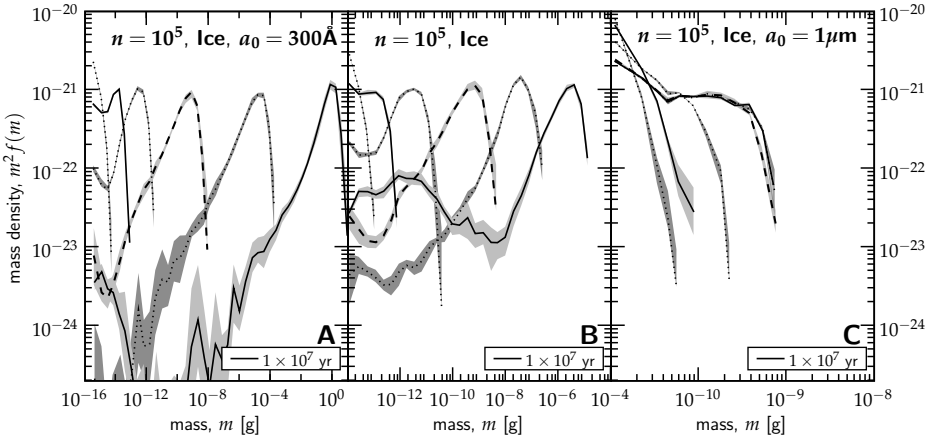

Figure 6.13 — Effects of a varying monomer size a_0 on the evolution of the size distribution for the ice-coated silicates of the standard model: (*a*) $a_0 = 300$ μm, (*b*) $a_0 = 0.1$ μm (the default, shown for reasons of comparison), and (*c*) $a_0 = 1$ μm. To facilitate the comparison, physical units are used (grams) for the mass of aggregates, rather than the dimensionless number of monomers (N).

ture this is often characterized by an impact strength Q, which is the ratio of the excavated mass over the collision energy. Changing the monomer size will affect the strength of the monomers, because it determines the amount of surface area that must be broken. Taking the breaking energy as a typical threshold for fragmentation, we obtain $Q \sim E_{\rm br}/m_0 \sim 10^7$ erg g^{-1} for $a_0 = 0.1$ μm size aggregates and a scaling with size of $Q \propto a_0^{-5/3}$. Therefore, aggregates that consist of smaller grains are much more resistant against energetic collisions than aggregates consisting of larger monomers. Likewise, silicate grains due to their much lower γ have a correspondingly lower strength. We do point out that in reality Q must be determined by experiment; however, our definition ($Q \sim E_{\rm br}/m_0$) serves explanatory purposes.

These effects are best seen in Fig. 6.13c where a tenfold increase in monomer size compared to the standard model (Fig. 6.13b) results in completely different distribution curves. Due to the much reduced strength of the aggregates, fragmenting collisions occur already from the outset. The curves, therefore, resemble the silicate models of Fig. 6.12b, which are also dominated by fragmentation. Figure 6.13a, on the other hand, shows the effects of reducing the size of the monomers by about a factor three ($a_0 = 0.03$ μm). Despite starting out at a lower mass, the 300 Å model quickly catches up with the standard model and overtakes it at $t \sim 10^6$ yr. This results because significant compaction fails to occur, in line with the results of the simple analytic model of Sect. 6.5.1; until 4×10^6 yr no significant compaction takes place, and aggregates become really

Table 6.6 — The mass-weighted size of the distribution, $\langle a \rangle_m$, at several distinct events during the simulation run. Col. (1) list the models in terms of the density (n) and material properties. The monomer size (a_0) is 0.1 μm, unless otherwise indicated. Cols. (2)–(5) give the mass-weighted size of the distribution at fixed coagulation times. Likewise, cols. (6)–(7) give value of $\langle a \rangle_m$ at the free-fall and the ambipolar diffusion timescale of the cloud that corresponds to the gas density n. These are a function of density and are given in Eq. (6.1) and Eq. (6.4), respectively. Values $a \times 10^b$ are denoted $a(b)$.

	$\langle a \rangle_m$ [cm]					
model	10^4 yr	10^5 yr	10^6 yr	10^7 yr	$t_{\rm ff}(n)$	$t_{\rm ad}(n)$
(1)	(2)	(3)	(4)	(5)	(6)	(7)
$n = 10^3$, ice	1.0(−5)	1.0(−5)	1.2(−5)	8.3(−5)	1.2(−5)	8.3(−5)
$n = 10^4$, silicates	1.0(−5)	1.1(−5)	1.4(−5)	1.4(−5)	1.2(−5)	1.4(−5)
$n = 10^4$, ice	1.0(−5)	1.1(−5)	4.6(−5)	8.5(−4)	1.5(−5)	8.5(−4)
$n = 10^5$, silicates	1.0(−5)	1.9(−5)	4.0(−5)	4.0(−5)	2.0(−5)	4.0(−5)
$n = 10^5$, silicates, $a_0 = 10^{-4}$	1.0(−4)	1.0(−4)	1.0(−4)	1.0(−4)	1.0(−4)	1.0(−4)
$n = 10^5$, ice	1.0(−5)	2.2(−5)	6.4(−4)	7.4(−3)	2.3(−5)	3.2(−3)
$n = 10^5$, ice, $a_0 = 10^{-4}$	1.0(−4)	1.1(−4)	2.2(−4)	2.3(−4)	1.1(−4)	2.3(−4)
$n = 10^5$, ice, $a_0 = 3 \times 10^{-6}$	3.2(−6)	1.1(−5)	1.3(−3)	4.3	1.2(−5)	2.4(−1)
$n = 10^5$, ice, compact	1.0(−5)	1.5(−5)	1.4(−4)	5.8(−3)	1.6(−5)	1.3(−3)
$n = 10^5$, ice, head-on	1.0(−5)	2.2(−5)	3.6(−4)	7.5(−3)	2.4(−5)	3.1(−3)
$n = 10^6$, silicates	1.4(−5)	1.2(−4)	1.3(−4)	1.3(−4)	4.4(−5)	1.3(−4)
$n = 10^6$, ice	1.4(−5)	2.7(−4)	3.7(−2)	2.0(−2)	4.6(−5)	2.9(−2)
$n = 10^7$, ice	7.9(−5)	3.7(−2)	5.2(−2)	6.1(−2)	8.6(−5)	7.8(−1)

porous indeed ($\phi \simeq 4 \times 10^{-4}$). The consequence is that fragmentation is also delayed, and has only tentatively started at the close of the simulations.

Tables 6.6 and 6.7 present the results of the coagulation/fragmentation process in tabular format. In Table 6.6 the mass-weighted size of the distribution (reflecting the largest particles) are given, and in Table 6.7 the opacity of the distribution is provided, which reflects the behavior of the small particles. Here, opacity means geometrical opacity – the amount of surface area per unit mass – which would be applicable for visible or UV radiation, not to the IR. Its definition is, accordingly,

$$\langle \kappa \rangle = \frac{\sum \pi a_i^2}{\sum m_i}, \tag{6.38}$$

where the summation is over all particles in the simulation. These tables show, for example, that in order to grow chondrule-size particles ($\sim 10^{-3}$ g), dust grains need to be ice-coated and, except for the $n = 10^6$ cm^{-3} model, coagulation times of $\sim 10^7$ yr are required. Furthermore, concerning the observational properties, Table 6.7 shows that a decrease of the opacity by a factor of 10 at most can be expected, for ice models at long timescales.

Table 6.7 — Like Table 6.6 but for the geometrical opacity of the particles. The opacity κ gives the total surface area per unit (dust) mass.

	$\langle\kappa\rangle$ [cm^2 g^{-1}]					
model	10^4 yr	10^5 yr	10^6 yr	10^7 yr	$t_{\rm ff}(n)$	$t_{\rm ad}(n)$
(1)	(2)	(3)	(4)	(5)	(6)	(7)
$n = 10^3$, ice	2.8(4)	2.8(4)	2.7(4)	1.5(4)	2.7(4)	1.5(4)
$n = 10^4$, silicates	2.8(4)	2.8(4)	2.7(4)	2.6(4)	2.7(4)	2.6(4)
$n = 10^4$, ice	2.8(4)	2.8(4)	2.0(4)	2.5(3)	2.6(4)	2.5(3)
$n = 10^5$, silicates	2.8(4)	2.5(4)	2.0(4)	2.0(4)	2.5(4)	2.0(4)
$n = 10^5$, silicates, $a_0 = 10^{-4}$	2.8(3)	2.8(3)	2.8(3)	2.8(3)	2.8(3)	2.8(3)
$n = 10^5$, ice	2.8(4)	2.4(4)	5.1(3)	2.3(3)	2.4(4)	8.4(2)
$n = 10^5$, ice, $a_0 = 10^{-4}$	2.8(3)	2.8(3)	2.4(3)	2.4(3)	2.8(3)	2.4(3)
$n = 10^5$, ice, $a_0 = 3 \times 10^{-6}$	9.3(4)	7.1(4)	1.4(4)	4.4(2)	6.9(4)	1.7(3)
$n = 10^5$, ice, compact	2.8(4)	2.6(4)	8.0(3)	1.9(3)	2.6(4)	1.0(3)
$n = 10^5$, ice, head-on	2.8(4)	2.4(4)	4.9(3)	3.1(3)	2.4(4)	9.3(2)
$n = 10^6$, silicates	2.7(4)	1.4(4)	1.4(4)	1.4(4)	2.0(4)	1.4(4)
$n = 10^6$, ice	2.7(4)	1.2(4)	6.7(2)	2.2(3)	2.0(4)	1.5(3)
$n = 10^7$, ice	1.7(4)	1.8(3)	1.4(3)	1.7(3)	1.6(4)	6.4(2)

6.6 Assessment of the collision recipe

Our study of coagulation in Molecular Clouds is the first study that applies the results of detailed numerical simulations – simulations, that have previously succeeded in explaining laboratory experiments (Paszun and Dominik 2008b) – to the global evolution of molecular clouds. This includes modeling the impact parameter and porosity of aggregates as independent variables. Much effort has been invested in the collision model. Fragmentation, especially, is modeled in detail, being characterized by three parameters and distinguished through the local and global recipe. In summary, we have presented the first model that couples the collisional growth of aggregates to the evolution of their internal structure while simultaneously accounting for the diverse collision outcomes that follow from the changing velocities between the particles as they grow. The collision model, certainly, is state-of-the-art.

The drawback of relying on a sophisticated numerical model is, however, that their results are in the strictest sense only applicable to the same size regime, i.e., for $N \lesssim 10^3$ particles. For silicates, this limited dynamic range of the numerical models is appropriate, because coagulation does not proceed beyond $N \sim 10^3 - 10^4$ (Fig. 6.12). Ice grains, on the other hand, are capable to grow to much larger sizes. For the recipe to become applicable for these large aggregates *extrapolation* of the results of the collision experiments is required. This is a critical point of the recipe in which we have invested considerable effort. The outcome was that we divided collisions in two groups – local and global – scaled their results to the critical energies involved ($E_{\rm br}$ and $E_{\rm roll}$), and the number of

particles (either the total number, $N_{\rm tot}$, or the reduced number, N_μ). The idea behind these normalizations is to make the collision recipe scale-independent: applicable to the low-N regime as well as the large-N regime.

Extrapolating the collision recipe nonetheless risky. Because of the large dynamic range involved and the embedding of the results in a MC approach, collisions of many small particles with a large particle are considered simultaneously through the grouping method. Tiny deviations of the recipe then have the potential to blow up. Furthermore, the extrapolation assumes that the collision physics at large scale is the same to the size of the collision experiments. This, too, is a crucial assumption in which collisional outcomes like *bouncing* are *a priori* not possible because these do not take place at the low-N part of the simulations.

Below, we present some of the limitations of the collision recipe, and offer suggestions for future improvement. These points concern the physics represented in the collision recipe (bouncing, irregular grains, and a size distribution of grains) or its implementation into a coagulation model. Although we acknowledge that by including a more sophisticated treatment, it is probable that the quantitative outcome of the collision experiments will change to some extent, we do not expect that the main results of our model – the initial coagulation phase, followed by the transition to a flat steady-state distribution – and their dependence on gas density and material properties will be much affected.

6.6.1 Bouncing

Bouncing of aggregates is observed in laboratory experiments (Blum and Muench 1993; Blum 2006), whereas it does not occur in our simulations. For silicates, the bouncing phenomenon occurs at sizes above approximately 100 μm (i.e., $N > 10^9$ particles) and is not fully understood. It is a challenge to investigate in the laboratory the microphysics of these large particles.

In the case of ice-coated silicate grains, which provide stronger adhesion forces, our simulations show that growth proceeds to $\sim$100 μm sizes where bouncing becomes potentially important. In this case, therefore, the growth might slow down earlier than observed in our experiments, especially when the internal structure has already re-adjusted to a compact state, where energy dissipation is no longer available. It is presently unclear how these laboratory experiments apply to ice aggregates and hence whether and to what extent the Monte Carlo results would be affected by bouncing. We recognize that this may, potentially, present a limitation to growth of aggregates in molecular clouds, but also emphasize it will not affect the main conclusions from this study as in only few models aggregates grow to sizes $\gg$100 μm.

6.6.2 Size distribution of grains

Our recipe is based on simulations of aggregates that are built of monomers of a single size. Therefore, we treat a monodisperse distribution. However, ISM-

dust typically consist of a size distributions of small grains and larger grains. The most frequently used size distribution is the MRN-distribution where the grain distribution scales as a $-7/2$ power-law of size, between a lower (a_i) and an upper (a_f size) (Mathis et al. 1977). Thus, in the MRN-distribution the smallest grains are dominant by number, whereas the larger grains dominate the mass. For an MRN distribution we take, $a_\mathrm{i} = 50$ Å and $a_\mathrm{f} = 0.25$ μm. Therefore, the collision outcome may differ when the colliding particles are made of grains of several sizes.

To illustrate this point, we quantitatively compare the aggregates' strength for a monodisperse and an MRN size distribution using the Q prescription. As described in Sect. 6.5.2 the strength of aggregates is determined by the breaking energy, which scales proportional to the contact radius as $E_\mathrm{br} \propto a_\mu^{4/3}$. We will assume that in the MRN distribution a typical contact area always involves a small grain, so that we can substitute $a_\mu = a_i$ in the E_br expression. Next, we assume that the number of contacts is of the order of the number of grains. Then, in order to determine their strength, we calculate the number of grains per unit of mass,

$$\frac{N}{m} \propto \frac{\int_{a_i}^{a_f} n(a)\mathrm{d}a}{\int_{a_i}^{a_f} n(a)a^3\mathrm{d}a} \simeq a_\mathrm{f}^{-1/2} a_\mathrm{i}^{-5/2}/5, \tag{6.39}$$

where we have used that $a_\mathrm{f} \gg a_\mathrm{i}$. In the monodisperse case, the equivalent quantity is $(N/m)_0 \propto a_0^{-3}$.

The strength of the MRN-grains can then be estimated by considering the energy dissipation per unit of mass. Thus, we multiply their typical breaking energy, which from the reasons given above is determined by the smallest grains a_i, by N/m. Comparing this to the monodisperse case we obtain

$$\frac{Q_\mathrm{MRN}}{Q_0} = \frac{a_i^{4/3}(N/m)_\mathrm{MRN}}{(a_0/2)^{4/3}(N/m)_0} = \frac{\frac{1}{5}a_\mathrm{f}^{-1/2}a_\mathrm{i}^{-7/6}}{(\frac{1}{2})^{4/3}a_0^{-5/3}} \simeq 0.5\left(\frac{a_f}{a_0}\right)^{-1/2}\left(\frac{a_0}{a_i}\right)^{7/6}. \tag{6.40}$$

(Note again that this calculation assumes that $a_\mathrm{f} \gg a_\mathrm{i}$; otherwise the numerical prefactor would be different.) In our study, where the monomer size was mostly fixed at $a_0 = 0.1$ μm, this ratio is about 10. Equation (6.40) therefore shows that the size distribution can increase the strength of an aggregate. In this picture, small grains act as the 'glue' that holds the bigger grains together and efficiently absorbs the incoming energy, because there is more contact surface. This occurs only if small monomers dominate by number. Otherwise, the mass dominated by big grains is held by much weaker contacts provided by small grains.

The results above show that in our standard case of $a_0 = 0.1$ μm the strength of aggregates is underestimated by a factor of ~10, compared to the MRN-distribution. In the case of $a_0 = 0.03$ μm, the aggregate strength would be approximately the same as an MRN-distribution of grains. Remark, finally, that the above analysis only concerns the intrinsic strength of aggregates, not the relative velocities. These are determined by the friction times of the particles

and the question therefore is how a distribution of grains affect the filling factor of aggregates, or, rather, the mass-to-surface area of aggregates. These will be active areas of future research.

6.6.3 Irregular particles

In this study we approximate grains with spheres, because irregular monomers are virtually impossible to simulate. Numerical modeling of these randomly shaped particles is very difficult and computationally expensive. Here, we try to assess the effect of irregular grains on the strength of aggregates and on the collision outcome.

The strength of an aggregate can be defined as the amount of the contact area per mass that is held by these inter-grain connections. The contact size in the case of irregular monomers depends on the radius of curvature local to the place where the grains touch each other. Therefore, highly irregular grains are held by contacts of much smaller size, because they are connected by surface asperities. This must result in a much weaker strength of aggregates. On the other hand, irregular monomers may form more than one contact with each other. This results in a higher restructuring threshold, as the energy required to initiate rolling is comparable to the energy needed to break a contact.

Poppe et al. (2000) determined the critical sticking velocity for monomers of different size, shape, and material properties. They showed that irregular enstatite grains can stick at much higher velocities than silica spheres, $5 - 25$ m s^{-1} for enstatite and $1.5 - 2.3$ m s^{-1} for silica. This discrepancy suggests that additional energy dissipation may occur during a collision. The mechanism that allow sticking at this high velocity remains unknown.

Since the physical processes that determine the behavior of irregular monomers are not fully understood, we leave this issue to further study. We remark, however, that the geometry of the grains does not pose a bottleneck to the validity of the collision model; instead the consequences of irregular monomers will merely be reflected in a different energy scaling.

6.6.4 Structure of particles

In the recipe the internal structure of particles is described by only one parameter: the geometrical filling factor, ϕ_σ. Thus, in our model the full structure of an aggregate follows from ϕ_σ. Therefore, the collision model always assumes a spherically symmetric structure, despite the fact that elongation appears in the output results of the numerical model, especially in grazing collisions. Moreover, the filling factor is an averaged quantity and does not determine whether the aggregate structure is homogeneous or fractal; e.g., the structure of a PCA particle is very different from a $D_\mathrm{f} = 2$ fractal but they can have the same filling factor if N is small. However, these are mostly second order effects and to use more variables that describe the internal structure requires a significant increase in the load of the recipe model.

6.6.5 The tabular format

In Appendix 6.8 the tabular format of the recipe is discussed at length. The tabular format was first presented in the Paszun and Dominik (2008a) study, but here additional tables were required in order for the recipe to become applicable to the MC program. The alternative would have been to provide analytic fits that would depend on three parameters (energy, impact parameter, and porosity). Fits have the advantage that the behavior of the low and high energy regimes are immediately evident; indeed, it would become easier to include boundary constraints from an analytical prescription. However, providing 3D-analytical fits turned out to be impractical, particularly because phenomena as restructuring are somewhat erratic in nature. On the other hand, the advantage of the tabular format is that the results are implemented in the recipe in a straightforward and unbiased way.

6.7 Discussion

As can be seen from Tables 6.6 and 6.7 coagulation of bare silicates only marginally affects the collisional evolution. Therefore, we do not expect that coagulation of bare silicates in molecular cloud cores will leave significant imprints on either the large particles or the observational diagnostics. At $T \sim 10$ K we do consider ice-coating of grains the more relevant scenario, however. Freeze-out of H_2O-ice on grains proceeds at thermal motions and is therefore faster than coagulation, provided the dust particles are well-shielded from UV-photons (Bergin et al. 1995). Then, our results suggest that grains have the potential to grow significantly, if densities are high and long coagulation timescales are available ($\gtrsim 10^6$ yr). But do these conditions materialize in molecular clouds? We will address these questions and compare our results to previous studies on dust coagulation in molecular clouds.

Ossenkopf (1993) and Weidenschilling and Ruzmaikina (1994) have pioneered studies of dust coagulation in molecular clouds. As is the case with this study, these models contain significant detail. Ossenkopf (1993) includes a structural parameter (essentially the geometrical filling factor, ϕ_σ), an MRN size distribution for the initial distribution of dust particles (covering the range of 50 – 2500 Å), and presents a model for the change in collisional properties upon collisions for the hit-and-stick regime. The model of Ossenkopf (1993), however, does not include aggregate restructuring and fragmentation and is therefore only applicable to the first stages of coagulation. Ossenkopf (1993) evolves his models for $\sim 10^5$ yr, usually at rather high densities ($n \gtrsim 10^6$ cm^{-3}) for which fragmenting collisions between ice(-coated) particles are indeed of no concern. The coagulation then proceeds to produce particles of compact size, ~ 0.5 μm. It can be seen from Table 6.6 that the growth in the corresponding model of our study (ice, $n = 10^6$) is higher: 1.9 μm. This may be caused by the somewhat lower turbulent velocities Ossenkopf (1993) adopts and, the fewer big ~ 0.1 μm grains

the MRN distribution contains compared to our monodisperse models. At any rate, the study of Ossenkopf (1993) is mainly focused on understanding the IR dust-opacities during this relatively short timescale (Ossenkopf and Henning 1994).

On the other hand, Weidenschilling and Ruzmaikina (1994) evolve their models for much longer timescales, until $t = 10^7$ yr. Like our study, Weidenschilling and Ruzmaikina (1994) include fragmentation in the form of erosion and, at high energies, shattering. Their particles are characterized by a strength of $Q \sim 10^6$ erg g^{-1}, which are, therefore, somewhat weaker than the particles of our standard model. Although their work lacks a dynamic model for the porosity evolution, it is assumed that the initial growth follows a fractal law until 30 μm. At these sizes the minimum filling factor then becomes less than 1%, lower than in our models.

Weidenschilling and Ruzmaikina (1994) model a Bonnor-Ebert sphere where the density at the inner region is ten times higher than at the surface. They find that the coagulation proceeds initially faster at the lower density outer regions than inside the cloud. This is caused by the assumption that the turbulent pressure stays the same throughout the cloud, providing higher turbulent motions in the outer regions. Still, coagulation is significant. Particles grow to $\gtrsim$100 μm in their nominal model at timescales of $\sim 10^6$ yr, which is comparable to our standard model. More striking is that the nature of the growth is different: while in our model the mass-peak always occurs at the high-mass end of the spectrum, in the Weidenschilling and Ruzmaikina (1994) calculations most of the mass stays in the smallest particles. In this respect, our findings qualitatively agree with the coagulation-fragmentation model of Brauer et al. (2008a) for protoplanetary disks. In contrast, the lack of massive particles in the Weidenschilling and Ruzmaikina (1994) models may be a result of the diffusion processes Weidenschilling and Ruzmaikina (1994) include; massive particles produced at high n mix with less massive particles from the outer regions.

Thus, although the models agree on the amount of growth that is obtained, there is some difference in detail, which result from the different collisional behavior of aggregates as well as the adopted cloud model.

In our models we observe that the shape of the initially monodisperse dust size distribution evolves rapidly, first to a Gaussian-like distribution and eventually to a flat steady-state distribution. For timescales longer than the coagulation timescale (Eq. (6.16)) we can expect that this result is independent of the initial conditions, even if the coagulation starts from a power-law distribution. Essentially, these distributions are a direct result of the physics of the coagulation: the Gaussian-like distribution reflects the hit-and-stick nature of the agglomeration process at low velocities while the flat $f(N)N^2$ distribution at later times results from a balance between fragmentation – erosion but not catastrophic destruction – and growth. In contrast, in interstellar shocks grains acquire much larger relative velocities and grain-grain collisions will then quickly shatter aggregates into their constituent monomers (Jones et al. 1996). Hence, the inter-

stellar grain size distribution will be very different in the dense phases of the interstellar medium than in the diffuse ISM and studies of the effects of grains on the opacity, ionization state and chemical inventory of molecular clouds will have to take this into account.

To further assess the impact of grain coagulation we must compare the coagulation timescales with the lifetimes of molecular clouds.

In a study of molecular clouds in the solar neighborhood Hartmann et al. (2001) hint the lifetime of molecular cloud is short, because of two key observations: *(i)* most cores do contain young stars, rather than being starless; and *(ii)* the age of the young stars that are still embedded in a cloud is 1 – 2 Myr at most. From these two arguments it follows that the duration of the preceding starless phase is also 1 – 2 Myr. Therefore, the grain population will not leave significant imprints on either *(i)* the large particles produced, or *(ii)* the removal of small particles, if core lifetimes are limited to the free fall time (Eq. (6.1)). This can be seen from Tables 6.6 and 6.7 where the growth in terms of the mass-weighted size ($\langle a \rangle_m$, Table 6.6) and the reduction of the geometrical surface (κ, Table 6.7) is given at the free-fall time of the simulation (col. 6). From Table 6.6 it is seen that the sizes of the largest particles all stay below 1 μm, except for the models that started off at monomer sizes of $a_0 = 1$ μm. Similarly, Table 6.7 shows that the opacities from the $t_{\rm ff}$ entry (col. 6) are similar to those of the 10^4 yr column.

This information is also displayed in Fig. 6.14. In Fig. 6.14a the decrease of the opacity with respect to the initial opacity is, κ/κ_0, is plotted against time, normalized by the initial coagulation timescale, for all $a_0 = 10^{-5}$ cm ice-coated silicate models. The similarity of the curves for the first ~10 $t_{\rm coll,0}$ is in good agreement with the simple analytic model presented in Sect. 6.5.1. In the models where small particles are replenished by fragmentation, κ first obtains a minimum and later levels-off at $\kappa/\kappa_0 \sim 0.05$. In Fig. 6.14b the coagulation timescale is plotted as function of gas density (dashed lines), where the solid black line shows the free-fall time (Eq. (6.1)). Open circles denote the time required to reduce the opacity by a factor e; filled circles by a factor $e^2 \sim 7$, and black cubes refer to a third e-fold reduction (~20). At $n = 10^3$ cm^{-3} the opacity is not reduced by even a single e-folding factor within 10^7 yr, and no symbols are shown at this density. At the free-fall timescale, no significant reduction occurs and the dust coagulation will not affect the chemistry in the dense core.

However, there is still lively debate whether the fast SF picture – or, rather, a fast timescale for molecular clouds – is generally attainable, as cores may have additional support mechanisms. If clouds are magnetically supported, the fast collapse phase is retarded by ambipolar diffusion. Then, star formation takes place on a much longer timescale, perhaps 10^7 yr (see Eq. (6.4)), much longer than the free-fall timescale. Thus, if ions couple to the magnetic field and retard the collapse, growth can be significant. Table 6.6 shows grains are then able to reached chondrule size proportions, ~100 μm, in the densest models. Also, the observational appearance of such a core will change significantly, as is clear from Fig. 6.14. If clouds exist on AD-timescales, Table 6.7 and Fig. 6.14 suggest

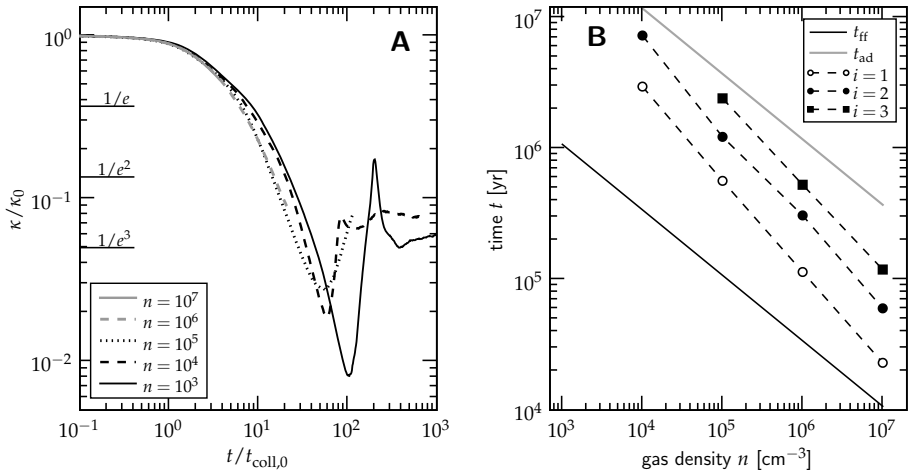

Figure 6.14 — (*dashed lines*) Coagulation timescales of the $a_0 = 0.1$ μm ice-coated silicates models at five different gas densities. (*a*) The opacity κ normalized to its initial value vs. time in units of the initial collision time $t_{\rm coll,0}$. The decrease in opacity occurs on timescales of $\sim 10\ t_{\rm coll,0}$. In the simulations that last long enough, however, κ starts to increase again, reflecting the re-emergence of small grains due to fragmentation. (*b, dashed curves*) Coagulation timescales in units of years as function of density. The timescales correspond to the point where the geometrical opacity, κ, has been reduced by a factor of $\exp[i]$ with $i = 1$ (open circles), $i = 2$ (filled circles) and $i = 3$ (squares), respectively. The free-fall timescale (Eq. (6.1)) and ambipolar diffusion timescale (Eq. (6.4)) are plotted for comparison by *solid lines*. If no symbol is plotted, the corresponding $i^{\rm th}$ *e*-folding reduction timescale has not been reached.

the UV-opacity, which is directly proportional to κ, will be reduced by a factor of ~ 10. In this case, studies that relate the $A_{\rm V}$ extinction measurements to column densities through the standard dust-to-gas ratio possibly underestimate the amount of gas that is actually present.

6.8 Conclusions and outlook

We have studied the collisional aggregation of dust in the environments of the molecular cloud (cores). In this study we have particularly focused on the collision model and the analysis of the collisional growth stages. Much effort was invested to apply the outcomes of the detailed numerical experiments to a collisional evolution model. We have treated a general approach, and outcomes of future experiments – either numerical or laboratory – can be easily included. One important feature of the collision model is its scaling to the relevant masses and critical energies, which allows the coagulation model to proceed to much larger sizes than covered by the original collision experiment. Our method is therefore also applicable to the dust coagulation and fragmentation stages in

protoplanetary disks.

In this study we discussed the observational implications of our model in a very coarse way, by considering the total amount of geometrical surface, captured in the κ parameter. We find that its behavior can be largely expressed as function of the initial collision timescale, $t_{\rm coll,0}$. It would be worthwhile to further investigate the extinction properties of the cloud as function of wavelength, and to quantify the importance of porous grains in it. Recently, Min et al. (2008) have presented a method to calculate the optical properties of porous aggregates, in which the filling factor is a key ingredient. In a follow-up study we will use this method in order to e.g., study the consequences of this study to the 10 μm silicate absorption feature.

We list below the key results that can be concluded from this study:

1. Coagulation can be roughly divided into two phases: a growth stage, where the $N^2 f(N)$ mass spectrum peaks at a well-defined size, and a fragmentation stage, where the $N^2 f(N)$ mass spectrum is relatively flat due to the replenishment of small particles by fragmentation. Fragmentation is primarily caused by erosive collisions.

2. A large porosity speeds up the coagulation of aggregates in the early phases. This effect is self-enhancing, because very porous particles couple very well to the gas, preventing energetic collisions capable of compaction. Grazing collisions are largely responsible for obtaining fluffy aggregates.

3. Silicates dust grains (without ice-coating) are always in the fragmentation regime. This is caused by their relatively low breaking energy.

4. The enhanced sticking capabilities of ices are conducive for growth. Likewise, a smaller grain size (or a distribution of grain sizes where small grains dominate the surface contacts) also enhance the growth phase.

5. If cloud lifetimes are restricted to free-fall times, little coagulation can be expected. However, if additional support mechanism are present and freeze-out of ice has commenced, dust aggregates of ~100 μm are produced, also significantly changing the UV-opacity of the cloud.